nature reviews methods primers

https://doi.org/10.1038/s43586-025-00425-8

Primer

Check for updates

Time-domain thermoreflectance

Ramya Mohan[1,6], Samreen Khan[2,6], Richard B. Wilson[2,3] & Patrick E. Hopkins[1,4,5]

Abstract

Time-domain thermoreflectance (TDTR) has been instrumental in measuring the heat transfer properties of bulk and nanostructured materials over the past two decades. In this Primer, we describe the optical and thermal aspects of TDTR, with an in-depth discussion on the theory, apparatus design and implementation. We present examples that illustrate the ability of TDTR to measure thermal conductivity tensors, thermal conductance across material interfaces, and volumetric heat capacity of thin films, 2D materials and bulk materials. The ability of TDTR to spatially resolve thermal properties is useful for studying heterogeneous material systems, such as materials processed in or subjected to extreme environments. We consider current limitations of pump–probe metrologies and discuss recent advancements of TDTR, such as time-resolved magneto-optic Kerr effect (TR-MOKE), beam-offset TDTR/TR-MOKE, steady-state thermoreflectance, frequency-domain thermoreflectance and laser-flash TDTR. Finally, we present an outlook on anticipated technological developments to further expand the ability of TDTR to measure nanoscale thermal properties.

Sections

[1]Department of Mechanical and Aerospace Engineering, University of Virginia, Charlottesville, VA, USA. [2]Department of Mechanical Engineering, University of California, Riverside, CA, USA. [3]Materials Science and Engineering Program, University of California, Riverside, CA, USA. [4]Department of Materials Science and Engineering, University of Virginia, Charlottesville, VA, USA. [5]Department of Physics, University of Virginia, Charlottesville, VA, USA. [6]These authors contributed equally: Ramya Mohan, Samreen Khan. e-mail: rwilson@ucr.edu; phopkins@virginia.edu

Introduction

Time-domain thermoreflectance (TDTR) is a laser-based experimental technique used to investigate thermal transport phenomena across various material systems[1,2]. TDTR monitors temperature-induced changes to a sample's reflectivity, known as thermoreflectance[3–6], caused by laser heating[3–6]. In a typical experiment, the sample is coated with a thin metal film (known as the transducer) that absorbs laser energy and converts it into heat. A time-delayed probe beam then measures the resulting changes in reflectivity[1,2]. Finally, experimental data are compared with the predictions of a thermal model[1], with one or two key thermal property parameters adjusted until the model accurately matches the observed behaviour.

TDTR confines the temperature rise to near-surface regions (spanning tens of nanometres to several micrometres[7]) by measuring the thermal response of materials on nanosecond to microsecond timescales. This surface-localized heating allows for the precise evaluation of thermal properties of thin films, material interfaces and microarchitectured materials (such as superlattices, hierarchically ordered nanocomposites and nanolaminates, among others). These nano-systems often exhibit transport properties that differ considerably from their bulk counterparts, on account of the mean free paths of heat carriers being altered by compositional defects, grain boundaries and strain[8–14].

The high lateral resolution of TDTR, typically ranging from 1 to 20 µm, enables detailed mapping of microstructural inhomogeneities or compositional gradients[15–21], and facilitates the characterization of thermal anisotropy in bulk and thin film systems, including 2D materials[22–25], multilayers[26–32] and porous organic frameworks[25,33–35]. Moreover, the lateral resolution of TDTR makes it possible to measure samples with sub-millimetre dimensions, such as exfoliated flakes of 2D materials[22–25], small crystals of next-generation semiconductors[36–41] and single polymer fibres[42]. TDTR is a non-contact experiment and has relatively simple sample preparation requirements, and therefore is a powerful tool for assessing the thermal properties of a wide range of materials and devices with complex geometries[43–53]. In short, TDTR and its experimental variations have proved over the past two decades to be a robust set of techniques for measuring the thermal properties of almost any material that can be prepared with an optically smooth surface.

Early innovations in pump–probe thermoreflectance have laid the groundwork for today's nearly standardized TDTR system, where both time-domain and frequency-domain thermal responses are exploited to enable thermal property measurements. The research groups of Eesley[54–56], Rosencwaig[57,58], Maris[59,60] and Rossignol[61] were among the first to report the use of pump–probe thermoreflectance techniques to study thermal and mechanical properties of thin films and interfaces. With the implementation of high repetition rate lasers (such as the now-standardized ~80 MHz Ti:sapphire oscillators, featuring <200 fs pulse widths), it becomes necessary to account for the effects of pulse accumulation on the measured signals[61–64]. The temporal spacing between pulses, $1/f_{rep}$, where f_{rep} is the laser repetition rate, is shorter than the time that the sample needs to cool to equilibrium after heating. As a result, heat from each pulse accumulates. Although these early studies recognized that pulse accumulation occurred, they still focused their analyses exclusively on the time-domain (or the in-phase) response to pulsed heating. As heat diffuses only a few tens to hundreds of nanometres over nanosecond timescales, this time-domain approach limits the sensitivity of measurements to the thermal properties of the underlying sample.

In the early 2000s, Cahill and co-workers introduced a breakthrough by decoupling the time-domain response from the accumulated signal[2,65–67]. Cahill mathematically demonstrated that an additional out-of-phase component, which relates the sample's thermoreflectance response to the modulated heating from the pump, could be analysed alongside the traditional in-phase response[1]. This breakthrough enabled pump–probe thermoreflectance measurements to access a wider range of time and length scales that are now sensitive to heat transfer processes that occur on the timescale of the modulation of the train of pump pulses (such as the out-of-phase signal), as opposed to only those that occur during the temporal decay after impulse heating from the pump pulse (such as the in-phase signal). Today, this innovation underpins the nearly standardized configuration of modern TDTR experiments, and is an important and powerful distinction between TDTR and other transient pump–probe techniques. Inspired by the definitions put forth by Koh et al.[68], we suggest that the term TDTR be reserved for experimental techniques where these in-phase and out-of-phase responses are used, whereas pump–probe techniques based on low-repetition rate lasers or continuous wave probe lasers should be termed transient thermoreflectance (TTR).

The primary focus of this Primer is to provide details of the experimental and analytical elements that define modern-day TDTR experiments. We first discuss the experimental set-up for TDTR (Figs. 1 and 2) and its variants. We then review principles for common measurements, such as thermal interface conductance, thermal conductivity tensors and heat capacities. Numerous basic TDTR principles reviewed here can be supplemented with the excellent TDTR tutorial by Jiang et al.[69]. Beyond that tutorial, this Primer includes an explanation of the physical meaning of TDTR signals, transducerless TDTR measurements, laser-flash TDTR and steady-state thermoreflectance (SSTR) while reviewing different applications of TDTR, such as for ion irradiation, spatial mapping, liquids and biomaterials.

A secondary focus of this Primer is to discuss advanced TDTR methods and related metrologies designed to address specific measurement challenges. For example, to measure the 3D thermal conductivity tensor of anisotropic materials, beam-offset TDTR uses offset pump and probe laser beams to resolve lateral heat spreading[70] (Fig. 1b). Time-resolved magneto-optic Kerr effect (TR-MOKE) leverages magneto-optic thermometry to improve sensitivity to in-plane and cross-plane thermal conductivity of thin films[71–73] (Fig. 1c), whereas laser-flash TDTR allows for measurements of the spatial evolution of the temperature profile in the through-plane direction as a function of time and heating frequency[74,75] (Fig. 1d). A comparative table outlining the operating principles, advantages and measurement limitations of TDTR and all of its variants is provided in Supplementary Table 1, along with critical sample preparation requirements for each technique. After discussing these experimental variations, we examine studies showcasing TDTR applications across diverse material systems. We provide best practices for data reproducibility, identify sources of error and consider experimental design factors. The Primer then explores the inherent limitations of TDTR in sampling representative volumes of material beneath a surface, and compares the technique with alternatives such as frequency-domain thermoreflectance (FDTR) and SSTR. Finally, the Outlook section explores emerging trends and considers future directions for TDTR and nanoscale thermal metrology.

Experimentation

Here, we provide an overview of the apparatus required for TDTR and describe the basic theory underpinning TDTR signals. Figure 2 shows the optical layout for a TDTR experiment, along with proposed modifications to the set-up that enable multiple measurement configurations

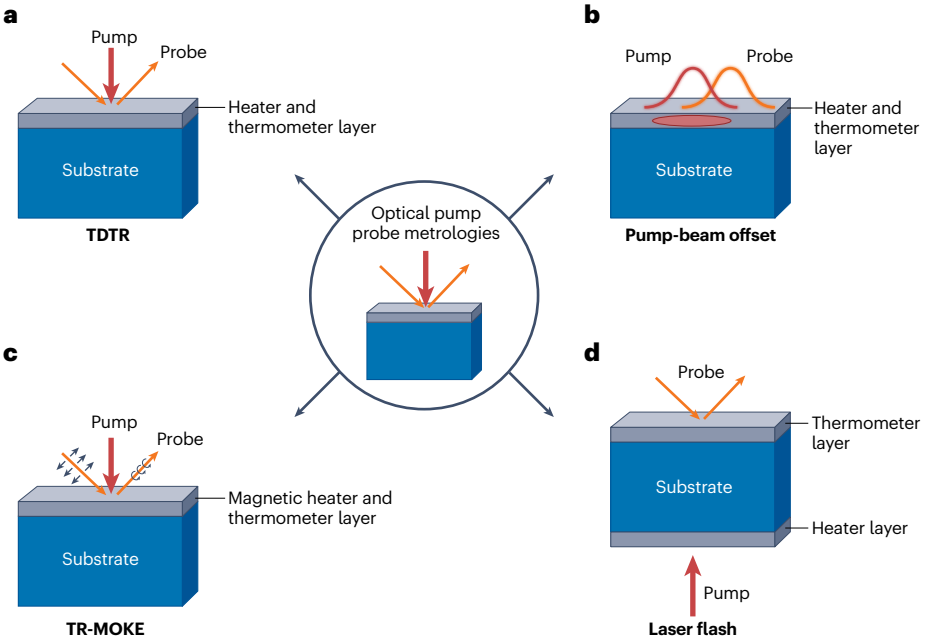

Fig. 1 | Introduction to optical pump–probe metrologies for thermal property measurements. **a**, Time-domain thermoreflectance (TDTR) measurements where the reflection geometry allows for thermal conductivity and heat capacity measurements of thin films and bulk samples. **b**, Beam-offset measurements where the heater and thermometer spots are offset by a specified distance. This geometry allows measurements of thermally anisotropic samples. **c**, Time-resolved magneto-optic Kerr effect (TR-MOKE) measurements. By substituting thermoreflectance with magneto-optic thermometry, this technique improves spatio-temporal resolution and allows measurements of thinner films. Beam-offset measurements can be performed in both TDTR and TR-MOKE configurations. **d**, Laser-flash measurements, where the heater and thermometer spots are on opposite sides of the substrate. By providing additional information about the temperature profile in the through-plane direction, laser flash is useful for multilayer samples with multiple unknown properties.

in a single optical table. We provide a detailed guide for building TDTR set-ups in Supplementary Note 1.

TDTR apparatus

Laser system. TDTR experiments typically use a solid-state diode-pumped Ti:sapphire oscillator that generates sub-picosecond pulses at a central wavelength of ~800 nm, with a spectral bandwidth of ~10–12 nm and a repetition rate of 80 MHz. If the output beam is elliptical, cylindrical lenses can be used to correct it[70]. In Supplementary Box 1, we provide an overview of Gaussian beam optics and associated formulae that are useful for beam shaping, beam collimation and focusing down to diffraction-limited spot sizes.

Delay stage. The delay stage controls the time delay between the pump and probe beams at the sample by introducing a controllable difference in path length. The delay stage can be placed in either the pump or probe path. Setting the delay stage on the pump path introduces a phase shift, $e^{i\cdot 2\pi\cdot f_{mod}\cdot t_{delay}}$, in the heating function that needs to be accounted for in the thermal modelling, where f_{mod} is the pump modulation frequency and t_{delay} is the pump–probe delay time[70]. The delay time is equal to the optical path length difference divided by the speed of light. The delay stage must introduce a path length difference of at least ≈0.9 m, yielding a delay time of at least ≈3 ns, so that the transducer–sample interface conductance, G, can be determined. G is measured by observing the timescale over which the metal film transducer's temperature decays, given by $\tau = h_t C_t / G$, where τ is the transducer's thermal response time, h_t is the transducer's thickness and C_t is the transducer's volumetric heat capacity. Typical values are $h_t = 10^{-7}$ m, $C_t = 3 \times 10^6$ J m^{-3} K^{-1} and $G = 10^8$ W m^{-2} K^{-1}, and thus τ is ≈3 ns.

Modulation of the pump beam. TDTR derives its sensitivity to the thermal properties of the sample by measuring the thermal response of the sample to harmonic heating at f_{mod}, and therefore modulation of the pump beam is necessary. An electro-optic modulator is used to modulate the train of pump pulses with typical modulation frequencies ranging between 0.1 and 20 MHz. The resulting heating function is shown in Fig. 3c. We discuss the effect of square and harmonic modulation envelopes in Supplementary Note 1.

Objective lens and integrated microscope. The pump and probe beams are focused onto the sample surface using an objective lens. Lenses with long working distances facilitate integration with sample environments such as optical cryostats or heater stages for in situ measurements. The probe beam must not be clipped at the back focal plane of the objective lens or anywhere on the optical path between the sample and the detector. Clipping the beam causes measurement artefacts by converting thermal expansion-induced phase modulations of the probe beam into intensity modulations[76–81]. This condition limits the size of the probe beam in free space, and consequently the diffraction-limited spot size on the sample (associated formulae can be found in Supplementary Box 1). An integrated microscope, composed of a charge-coupled device camera and a suitable lens, allows for sample surface imaging and ensures that the sample is reliably placed at the focal plane of the objective lens. Imaging of the surface also allows users to avoid regions of the sample with dust or defects and simplifies the spatial overlap of the pump and probe beams on the sample surface[82].

Detector and lock-in amplifier. The reflected probe beam is focused onto a silicon photodetector with a response time sufficient to resolve signals at f_{mod}. The detector is connected to a radio-frequency lock-in amplifier. The lock-in amplifier measures the amplitude and phase of the AC signal at f_{mod}. In Supplementary Note 1, we discuss design considerations for the detection circuit, and methods for blocking the pump beam from reaching the detector, which is critical.

Advanced TDTR methods

Beam-offset set-up. Precise control over the spatial overlap of pump and probe beams, known as the beam offset, is achieved either by using a goniometer with motorized actuators on the polarized beam-splitter (PBS) in front of the objective lens[70] or by utilizing motorized actuators

on a mirror in the pump beam path[83] (as shown in the red transparent box in Fig. 2a). Both of these methods deflect the pump beam by an angle of $\Delta\theta$ as it enters the objective lens producing a beam offset of $\Delta x_0 = F\Delta\theta$ on the sample surface, where F is the focal length of the objective lens. Offsetting the pump with respect to the probe allows the width of the in-plane temperature profile to be measured. In contrast to measurements with overlapped pump and probe beams, which depend on both through-plane and in-plane transport properties, the width of the in-plane temperature profile usually depends only on in-plane transport properties[70]. We discuss in-plane thermal conductivity measurements using beam offset in greater detail in 'Results'.

TR-MOKE set-up. The primary distinction between the TDTR and TR-MOKE experimental set-ups lies in the detector optics, as illustrated in Fig. 2b. TR-MOKE measures the magneto-optic Kerr effect, which describes the change in polarization of the reflected probe beam caused by the magnetization of a ferromagnetic transducer[84]. To measure the change in polarization, the reflected probe is split into orthogonally polarized components with a Wollaston prism and directed onto a balanced photodetector. Prior to the measurement, a half-wave plate (HWP) before the prism is rotated to balance the detectors. During the measurement, any temperature-induced changes in polarization imbalances the detectors and generates a signal proportional to the

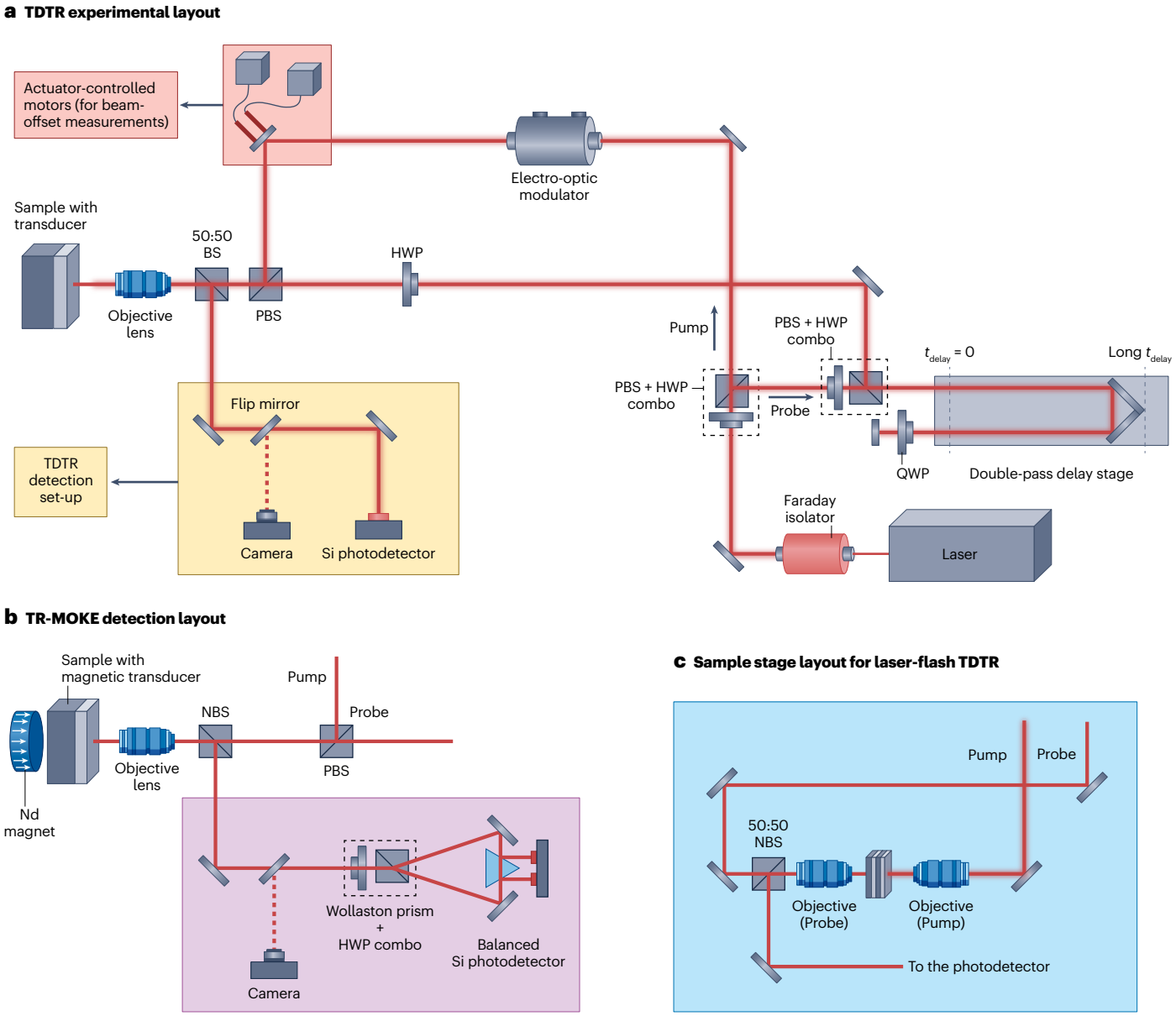

Fig. 2 | Optical schematic for time-domain thermoreflectance and experimental variants. a, Time-domain thermoreflectance (TDTR) experimental layout. A more detailed TDTR layout is shown in Supplementary Fig. 1. **b**, Detector layout for time-resolved magneto-optic Kerr effect (TR-MOKE) experiments. **c**, Sample stage design layout for laser-flash TDTR experiments. BS, beam-splitter; HWP, half-wave plate; NBS, normal beam-splitter; PBS, polarized beam-splitter; QWP, quarter-wave plate; t_{delay}, pump–probe delay time.

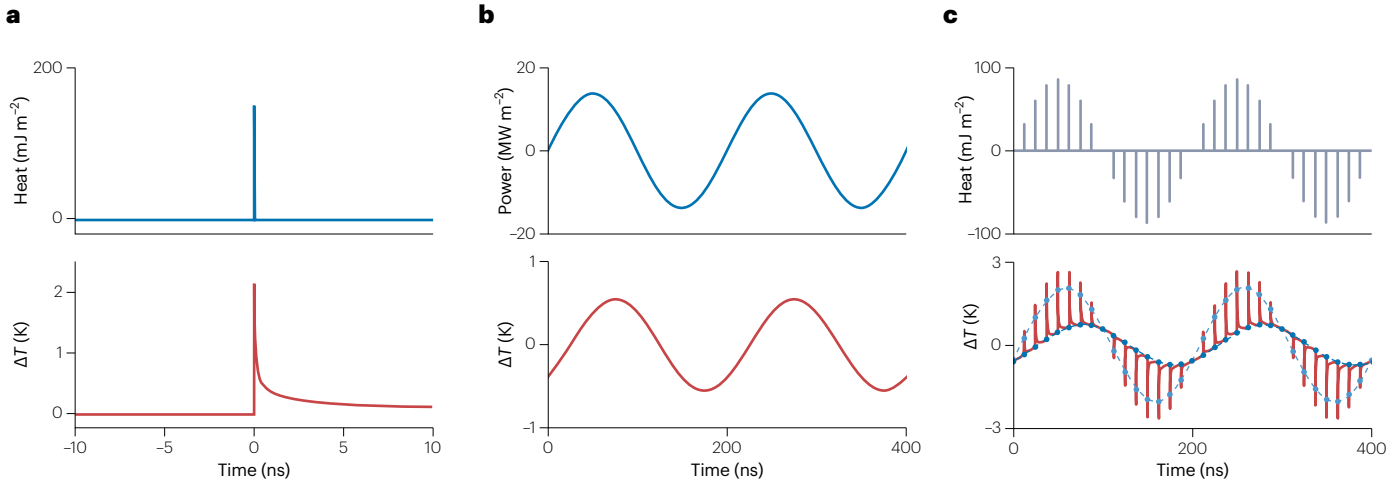

Fig. 3 | Thermal responses to different types of heating. a, Transient temperature rise following a single pump pulse. **b**, Temperature oscillation caused by harmonic heating at 5 MHz; the temperature waveform (red) lags the heating function. **c**, Temperature response to a pulse train whose envelope is modulated at 5 MHz (red curve). In a time-domain thermoreflectance (TDTR) experiment, measurements are collected over a series of delay times to gain information about both the harmonic response and the pulsed response. The probe samples the instantaneous temperature at fixed delays after each pump pulse: dark blue markers at −100 ps and light blue markers at +100 ps. The −100 ps trace is similar to the harmonic temperature response in panel **b** and describes the thermal response of the sample on a $1/f_{mod}$ timescale. Alternatively, the amplitude of the waveform at +100 ps reflects the pulsed response shown in panel **a** at a time 100 ps after the pulse. ΔT, excess surface temperature of the sample caused by heating; f_{mod}, pump modulation frequency.

temperature change. To suppress any thermoreflectance signals, it is useful to repeat the measurement with the transducer oppositely magnetized and taking the difference of the two signals. The resulting TR-MOKE ratio of in-phase to out-of-phase voltages can then be analysed identically to a conventional TDTR measurement.

As illustrated in Fig. 2b, TR-MOKE measures the real part of the ferromagnetic metal's Kerr rotation angle. The signal can sometimes be improved by instead measuring the imaginary part of the Kerr angle or some linear combination of the two. This can be accomplished by replacing the HWP before the prism with a quarter-wave plate (QWP)[85], or by adding a Babinet–Soleil compensator before the HWP[83]. In 'Results', we describe how TR-MOKE can enable superior sensitivity to both in-plane and through-plane transport coefficients.

Laser-flash TDTR set-up. Laser-flash TDTR involves heating and probing a sample on opposite sides to measure the cross-plane heat transfer as a function of time and/or heating frequency. The modified optical layout for laser-flash TDTR is shown in Fig. 2c. The pump beam path remains identical to that in standard TDTR experiments, whereas the probe beam is redirected using mirrors to reach the opposite side of the sample. The resulting reflected probe is then directed to a photodetector. We discuss the ability of laser-flash TDTR to measure through-plane temperature profiles of multilayer stacks and amorphous thin films in 'Results'.

Signal acquisition and processing

Across all variations of TDTR, the voltage signal measured by the radio-frequency lock-in amplifier is given as follows:

$$V(t) = \varsigma P_{probe} \frac{dR}{dT} \Delta T\left(t_{delay}\right) \quad (1)$$

where ς represents a set-up-specific constant that is equal to the product of the transmissivity of all the optical elements between the sample and the detector, the detector's responsivity and the gain of the electronics in the detection circuit[86]; P_{probe} is the power of the probe beam; dR/dT is the thermoreflectance coefficient of the transducer; and $\Delta T(t_{delay})$ is the lock-in measured temperature response as a function of pump–probe time delay. As we discuss below, ς, P_{probe} and dR/dT are not needed for typical analysis of TDTR data by considering both the in-phase and out-of-phase responses.

Lock-in signals (the in-phase voltage signal, V_{in}, and the out-of-phase voltage signal, V_{out}) are collected as a function of pump–probe time delay. Initially, data are collected over a short time-delay window, such as −20 to 100 ps, in small (~1 ps) increments. This first linear scan allows for the lock-in phase offset to be set and provides picosecond acoustics signals for film thickness determination (resolving picosecond acoustics signals requires pulse durations in the order of 1 ps or less[87]). Subsequent data are collected on a log scale from ~100 ps to the maximum delay time (typically ~4 ns). See Supplementary Fig. 2 for an outline of a basic TDTR measurement.

The lock-in amplifier measures the phase relative to a reference signal at f_{mod}, which is provided by the function generator. TDTR analysis requires the phase of the signal relative to the pump heating function to be known. As the phase of the pump heating function and reference signal will be different, a phase correction must be applied. This can be done during data analysis, or by adjusting the lock-in amplifier's phase setting manually. The optimal phase offset will flatten the out-of-phase signal near zero delay time, for example, making V_{out} constant from −20 to 20 ps. This is because the out-of-phase signal describes the thermal response on $1/f_{mod}$ timescales, which are not affected by a change of 40 ps in delay time. We suggest guidelines for choosing a suitable modulation frequency in Supplementary Note 2.

Signal theory

We now turn our attention to understanding and modelling the measured TDTR signals. The ratio of the V_{in} and V_{out} signals is analysed by

comparison with the predictions of the multilayer thermal model described by Cahill[1]. Prior studies provide detailed descriptions of the mathematics underpinning the multilayer thermal model for TDTR data analysis[1,7,71,88–91]. Here, we focus on building a physical intuition for the V_{in} and V_{out} signals.

TDTR's effectiveness arises from its ability to measure the response of the system to both pulsed heating and harmonic heating. We illustrate how this works in Fig. 3 by comparing thermal responses of a semi-infinite solid with thermal effusivity of $\approx 5 \times 10^3$ W s$^{0.5}$ m^{-2} K$^{0.5}$ from heating by a single laser pulse (Fig. 3a), by harmonic heating at 5 MHz (Fig. 3b) and by the modulated pulse train used in TDTR experiments with f_{mod} = 5 MHz (Fig. 3c). In Supplementary Note 2, we provide further details about the relationship of these three types of heating. Figure 3c (red curve) shows how the TDTR signal is constructed from the temperature evolution with time in response to modulated pulsed heating. The dark and light blue markers indicate the temperatures being sampled at a delay time of −100 ps and +100 ps, respectively. The harmonic function formed by these markers is detected by the lock-in at that time delay. The full TDTR signal is built by sampling the temperature across a range of time delays.

The V_{in} signal in a TDTR experiment corresponds to the temperature response synchronized (in-phase) with the pump modulation. It reflects the immediate temperature rise and the energy stored in the sample after each pump pulse. In other words, V_{in} describes the thermal response of the sample to heating from a single pulse, as illustrated in Fig. 3a. Notably, the harmonic function formed by the light blue markers at +100 ps in Fig. 3c is in phase with the modulation envelope. When the metal film (transducer) absorbs a single laser pulse, the magnitude of this temperature rise depends on the transducer's thickness and heat capacity. Subsequently, the transducer cools as heat flows into the sample beneath. The characteristic cooling time (τ) is governed by the interfacial thermal conductance (G) and the sample's thermal conductivity (k). Thus, the in-phase signal decays with time, and has an amplitude that is inversely proportional to the transducer's heat capacity per unit area: $V_{in} \propto f(t)/h_t C_t$, where the function $f(t)$ describes the decay rate. For samples with $k \gg h_t G$, the transducer can be treated as a lumped capacitance, and the temperature decays exponentially: $f(t) = \exp(-t/\tau)$.

Alternatively, the V_{out} signal lags the pump by 90°, and thus captures the delayed thermal response governed by heat diffusion away from the heated region. Here, the sample acts as a thermal integrator. Energy is deposited in discrete pulses but diffuses away slowly. As a result, V_{out} closely resembles what would be observed in response to continuous harmonic heating at frequency, f_{mod} (Fig. 3b,c). Notably, the harmonic function formed by the light blue markers at a time delay of −100 ps is similar in amplitude and phase to the harmonic temperature response caused by purely harmonic heating shown in Fig. 3b. In response to harmonic heating, the sample's temperature oscillates with an amplitude proportional to the thermal resistance of the sample across a characteristic length, d, defined as the distance that the heat diffuses during one modulation period $1/f_{mod}$. For bulk samples, this distance is the thermal penetration depth $d_p = \sqrt{k/\pi C f_{mod}}$ and $V_{out} \propto d_p/k$. Or, equivalently, V_{out} is inversely proportional to the sample's thermal effusivity: $V_{out} \propto 1/\sqrt{kC}$ (in Supplementary Note 2, we provide a more rigorous derivation of this heuristic).

In TDTR experiments, the ratio of V_{in} and V_{out} is analysed, which is convenient because it is independent of numerous experimental parameters that both V_{in} and V_{out} are proportional to, including ς, the transducer's dR/dT and the pump and probe powers. Based on the discussion above, the ratio for a TDTR measurement of a high-k bulk sample can be approximated as follows:

$$-\frac{V_{in}}{V_{out}} \approx \frac{2\sqrt{\pi f_{mod}}}{f_{rep}} \frac{\sqrt{kC}}{hC_t} \exp\left(\frac{-t}{\tau}\right) \quad (2)$$

For samples with low k, the amplitude will be the same, but $\exp(-t/\tau)$ will be replaced by a different decay function, $f(t)$, that depends on $h_t C_t$, G and $\sqrt{kC}$. A more detailed discussion and derivation of Eq. 2 is provided in Supplementary Note 2. The key points to take away from Eq. 2 are that the ratio signal in TDTR experiments usually scales with the sample's effusivity and the decay rate of the ratio signal provides a sensitive measure of the interface conductance between the transducer and the interface. We emphasize that although Eq. 2 is a useful heuristic for considering how changes in thermal properties will alter TDTR signals, actual data analyses are performed with the multilayer thermal model described in ref. 1.

FDTR is a technique closely related to TDTR. Both techniques measure the response of the sample to harmonic heating. In FDTR, the phase lag between the harmonic heating and thermal response (Fig. 3b) is measured as a function of heating frequency. In TDTR, the response to pulsed heating (Fig. 3c) is measured as a function of time delay normalized by the out-of-phase thermal response to harmonic heating at f_{mod}.

Sample preparation and choosing a transducer

TDTR experiments usually require coating the sample with a metal transducer. A metal transducer (>50 nm thick) in TDTR experiments confines heating and temperature sensing to the surface, prevents electron–hole pair excitation and simplifies thermal modelling by eliminating the need for depth-dependent absorption and thermoreflectance calculations[74]. The sample surface before and after transducer deposition needs to be smooth (for example, root-mean-square roughness of the surface <10 nm) to ensure no diffuse reflectance of the probe beam. Thus, not only must the interface between the sample and transducer be smooth but also the transducer must be deposited such that there are no elevated islands or raised grains formed on the surface. Supplementary Note 3 provides additional details about the role of the transducer and factors to consider during selection.

The figure of merit for maximizing the signal-to-noise ratio is $(1/R) \times (dR/dT)$ of the metal at the probe wavelength[86,92]. This value typically peaks at wavelengths near interband optical transitions[93], and is reported for various transducers[86,92]. Aluminium is a good transducer for most experiments with a probe wavelength near 800 nm, where it has large thermoreflectance, strong picosecond acoustic signals, high transducer thermal conductivity and good adhesion to most samples.

For in-plane thermal conductivity (k_r) measurements, the k_t value should be low. A high k_t value shunts the in-plane heat current. This reduces sensitivity to the sample's in-plane conductivity. Specifically, the transducer's in-plane conductance ($h_t \cdot k_t$) should be lower than the sample's in-plane conductance. The in-plane conductance of a thin film is $h_{film} \cdot k_{film}$, whereas for bulk samples it is $d_p \cdot k_{substrate}$. Metal alloys such as NbV ($k_t \sim 20$ W m^{-1} K^{-1})[71] or an AlTi bilayer ($k_t \sim 40$ W m^{-1} K^{-1})[94] combine low k with high dR/dT, which make them good transducer choices for in-plane measurements. Under specific experimental and material conditions, TDTR measurements can be conducted without metal film transducers (Supplementary Note 3).

Results

In this section, we describe measurement guidelines and results for the common types of TDTR experiments. These include measurements of thermal interface conductance, cross-plane thermal conductivity (k_z), in-plane thermal conductivity (k_r) and the volumetric heat capacity (C).

Thermal model parameters

A thickness h, volumetric heat capacity C and the cross-plane thermal conductivity k_z. The interfacial thermal conductance (G) between adjacent layers is also needed. In the specific case where d_p and the laser spot size (w_0) are comparable, heat transport becomes 3D (Fig. 4b) and the in-plane thermal conductivity (k_r) is also required, which is discussed later in this section. Finally, w_0 must be known for all TDTR measurements.

Typically, a single TDTR experiment measures two quantities: the ratio of pulsed to harmonic heating responses, $-V_{in}/V_{out}$, and its decay rate with time delay. As only two experimental quantities are measured, in most cases it is only possible to fit for two parameters when analysing a TDTR dataset at a single modulation frequency: the transducer–sample G and one additional parameter, such as the sample k value. All other parameters in the model must be independently determined. The parameters being fit should not be strongly coupled. For example, looking at Eq. 2, k and C are expected to be coupled in standard 1D TDTR measurements as they both affect the ratio in the same manner. Supplementary Fig. 4 shows the results of calculations done with the TDTR thermal model to determine whether two parameters are coupled.

For a 1D TDTR measurement ($w_0 \gg d_p$) (Fig. 4a), the ratio is most sensitive to the thermal capacitance of the transducer (h_tC_t)[95]. For TDTR measurements with a 3D temperature profile ($w_0 \sim d_p$) (Fig. 4d), the ratio is most sensitive to w_0 (refs. 70,95). Thus, these parameters must be precisely known or measured, so as to minimize uncertainties in the reported k and G values.

Measurements of thermal interface conductance and cross-plane thermal conductivity

The effect that a sample's k value has on TDTR signals is shown in Fig. 4c by comparing data and model fits for bulk diamond[96], 4H-SiC (ref. 96) and Al_2O_3 (ref. 73) with TiN transducers. The difference in k value for these samples translates into ratios that vary by about a factor of 10, because $-V_{in}/V_{out}$ scales with $\sqrt{k}$ (Eq. 2). The decay of the ratio with time delay provides a sensitive measure of the interface conductance with $G = 500$ MW m^{-2} K^{-1} for TiN/Al_2O_3 (ref. 73), $G = 750$ MW m^{-2} K^{-1} for TiN/4H-SiC (ref. 96) and $G = 400$ MW m^{-2} K^{-1} for TiN/diamond[96].

To show the effect that G has on the ratio, Fig. 4d compares the results of TDTR measurements of diamond with two different metal transducers: HfN[97] and TiN[96]. The thermal interface conductance differs by a factor of three, so for the TiN/diamond measurement the ratio decays much more rapidly with delay time t.

Thermal conductivity of thin films

TDTR is effective at characterizing the cross-plane transport properties of thin films. In general, TDTR measurements of thin films involve the determination of three thermal properties: the transducer–film interface conductance (G_1), the film thermal conductivity (k_{film}) and the film–substrate interface conductance (G_2). The ability of a TDTR measurement to independently determine these parameters depends on how the film thickness (h_{film}) compares with two other key length scales: d_p and the transducer thickness (h_t). We consider three limits and describe heuristics that are useful for designing experiments.

First, when h_{film} is less than h_t, TDTR measures a single lumped resistance: $1/G_1 + h_{film}/k_{film} + 1/G_2$. The strong coupling of the three parameters of interest occurs because TDTR works, in part, by analysing the timescale for cooling of the transducer after pulsed heating. For the transducer to cool, it must transfer heat into an adjacent region of comparable thickness[98]. Therefore, depth resolution of TDTR is inherently limited by h_t, making it challenging to resolve thermal resistances localized to regions thinner than h_t.

In the second case, when h_{film} is greater than h_t but less than d_p, the sensitivity of TDTR to the thermal conductivity of the film, k_{film} is coupled only to G_2. In this scenario, TDTR also measures an effective conductivity (k_{eff}): $h_{film}/k_{eff} = 1/G_2 + h_{film}/k_{film}$. The reason it is possible to separately determine k_{eff} from G_1 is because the sensitivity to G_1 is derived from the decay rate of the ratio with delay time (see τ in Eq. 2). Alternatively, k_{eff} is derived from the amplitude of the ratio signal (see k in Eq. 2). The differing depth sensitivities of V_{in} and V_{out} make it possible to independently determine G_1 and k_{eff}.

If the film's resistance, indicated by h_{film}/k_{film}, is much larger than the thermal interface resistances, it does not matter that these parameters are coupled, and $k_{eff} \approx k_{film}$. For k_{eff} to be within 20% of k_{film}, it is necessary for the film resistance to be at least approximately five times larger than the thermal interface resistances, which occurs when $h_{film} > 5k_{film}/G_2$. For a typical interface conductance value of $G_2 \approx 200$ MW m^{-2} K^{-1}, the minimum thickness for a film with k_{film} of 1, 3 and 10 W m^{-1} K^{-1} is 25, 75 and 250 nm.

Lastly, if h_{film} is greater than d_p, the heated region is confined to the film, and G_2 and the substrate thermal conductivity ($k_{substrate}$) have minimal impact on the observed signals. The maximum frequency possible in a TDTR experiment is typically ~20 MHz (ref. 99). Assuming a typical value for the film heat capacity of 2 MJ m^{-3} K^{-1}, the minimum film thickness, $h_{film} > \sqrt{k_{film}/\pi C_{film} f_{mod}}$, for films with k_{film} of 30, 100 or 300 W m^{-1} K^{-1} is 500, 900 and 1500 nm. When measuring high k_{film} on a low-k substrate, the minimum film thickness increases, such as $1.5d_p$ for copper on SiO_2 (ref. 98).

In the above discussion, we have described two minimum thickness criteria: the film should be thick enough that its thermal resistance dominates or the film should be thicker than the thermal penetration depth. Setting the two minimum film thickness criteria equal to one another yields $k_{film} = G_2^2/(25\pi C_{film} f_{mod})$. Using the values described above for G_2, C_{film} and f_{mod} yields $k_{film} \approx 13$ W m^{-1} K^{-1}. For films with k_{film} less than this value, it is easier to satisfy the dominant resistance condition. For films with k_{film} larger than this value, it is easier to satisfy the penetration depth condition.

For high-k_{film} films with $h_{film} > d_p$, it is sometimes possible to determine G_2 with a second TDTR measurement with a lower f_{mod} value[100]. The high frequency measurement is then analysed to determine k_{film} and G_1, and the lower frequency measurement can be analysed with only G_2 as a fit parameter. However, this approach requires the interface resistance $1/G_2$ to be comparable to $1/G_1$ and h_{film}/k_{film}, otherwise the uncertainty in G_2 will be large.

For scenarios where TDTR measures an effective film conductivity, the value of k_{film} can sometimes be isolated by measuring samples of various thicknesses[75,101–103]. The slope of total resistance versus thickness provides the intrinsic film conductivity, separating bulk conductivity from interface effects. However, this approach assumes that the

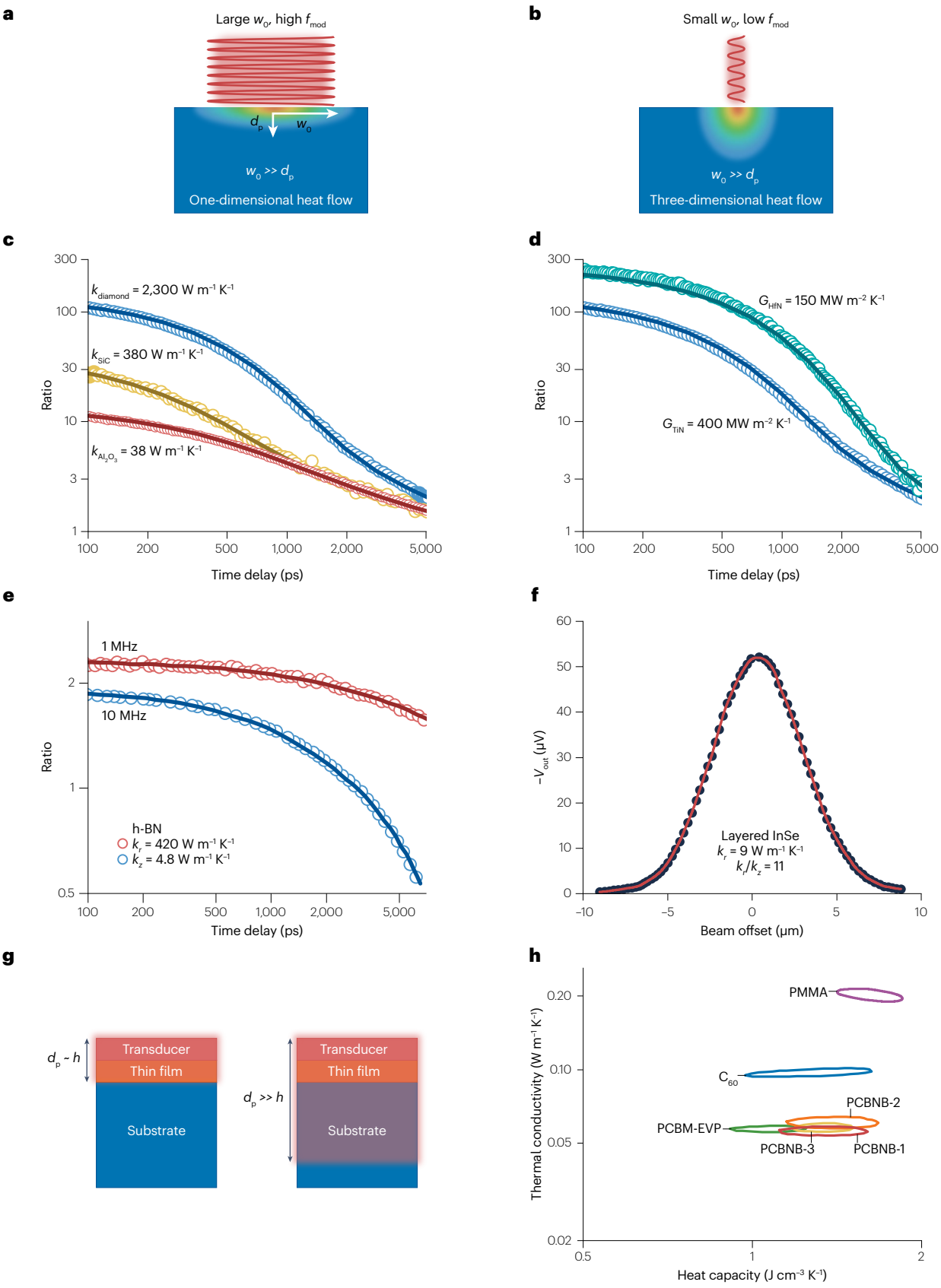
a
Large w_0, high f_{mod}
d_p
w_0
$w_0 >> d_p$
One-dimensional heat flow
b
Small w_0, low f_{mod}
$w_0 >> d_p$
Three-dimensional heat flow
c
$k_{diamond}$ = 2,300 W m^{-1} K^{-1}
k_{SiC} = 380 W m^{-1} K^{-1}
$k_{Al_2O_3}$ = 38 W m^{-1} K^{-1}
Ratio
Time delay (ps)
d
G_{HfN} = 150 MW m^{-2} K^{-1}
G_{TiN} = 400 MW m^{-2} K^{-1}
Ratio
Time delay (ps)
e
1 MHz
10 MHz
h-BN
k_r = 420 W m^{-1} K^{-1}
k_z = 4.8 W m^{-1} K^{-1}
Ratio
Time delay (ps)
f
$-V_{out}$ (μV)
Layered InSe
k_r = 9 W m^{-1} K^{-1}
k_r/k_z = 11
Beam offset (μm)
g
$d_p \sim h$
Transducer
Thin film
Substrate
$d_p >> h$
Transducer
Thin film
Substrate
h
PMMA
C_{60}
PCBNB-2
PCBM-EVP
PCBNB-3
PCBNB-1
Thermal conductivity (W m^{-1} K^{-1})
Heat capacity (J cm^{-3} K^{-1})

Fig. 4 | Representative data for common time-domain thermoreflectance experiments. a,b, Impact of modulation frequency and spot size on heat flow regimes in time-domain thermoreflectance (TDTR) experiments. At high modulation frequencies and large spot sizes, TDTR measures thermal effusivity under 1D heat flow conditions (panel **a**). Conversely, at low modulation frequencies and small spot sizes, TDTR captures thermal diffusivity in a 3D heat flow regime (panel **b**). **c**, Effect of sample thermal conductivity on TDTR signals. Markers indicate TDTR data for TiN-coated diamond, 4H-SiC and Al_2O_3. The lines are model predictions with thermal conductivity (k) and interfacial thermal conductance (G) treated as fit parameters. The magnitude of the ratio depends on the substrate's thermal conductivity, increasing with higher conductivity. **d**, Effect of the interface conductance on TDTR signals. The open markers indicate TDTR data for HfN/diamond and TiN/diamond. The decay of the ratio varies with the thermal interface conductance between the transducer and substrate, with higher conductance corresponding to a faster decay. **e**, TDTR data and thermal model fits for hexagonal boron nitride (h-BN) measured with a 10-μm spot size at modulation frequencies of 1 MHz and 10 MHz. The 10 MHz data were fit to extract the through-plane thermal conductivity, whereas the 1 MHz data were fit for the in-plane thermal conductivity. **f**, Out-of-phase signal as a function of beam offset for a 297 nm thick InSe flake (circles), with Gaussian thermal model fit (solid red line). **g**, Impact of modulation frequency on the thermal penetration depth relevant to heat capacity measurements of thin films. When $d_p < h$, the TDTR ratio is sensitive to both the heat capacity and the thermal conductivity of the thin film. When $d_p \gg h$, the heat capacity of the film becomes less relevant, but the ratio remains sensitive to the thermal conductivity of the film. **h**, Contour plots showing combinations of thermal conductivity and heat capacity that yield good fits by analysing measurements at both low and high modulation frequencies for fullerene (C_{60}), poly(methyl methacrylate) (PMMA), [6,6]-phenyl-C_{61}-butyric acid methyl ester (PCBM), highly disordered [6,6]-phenyl-C_{61}-butyric acid n-butyl ester (PCBNB)-1, crystalline phase I PCBNB-2 and crystalline phase II PCBNB-3. d_p, thermal penetration depth; f_{mod}, pump modulation frequency; k_r, in-plane thermal conductivity; k_z, cross-plane thermal conductivity; V_{out}, out-of-phase voltage signal; w_0, laser spot size. TiN/SiC and TiN/diamond data in part **c** and TiN/diamond data in part **d** adapted with permission from ref. 96, American Institute of Physics. TiN/Al_2O_3 data in part **c** adapted from ref. 73, CC BY 4.0. HfN/diamond data in part **d** adapted from ref. 97, CC BY 4.0. Part **e** adapted with permission from ref. 104, American Physical Society. Part **f** adapted with permission from ref. 106, American Institute of Physics. Part **h** adapted with permission from ref. 113, American Physical Society.

films of varied thickness have identical k_{film}, which is not always true. Crystal quality, and therefore k_{film}, can increase with film thickness as grains coalesce and defect densities decrease.

Frequency-dependent in-plane thermal conductivity measurements

TDTR measurements become sensitive to k_r when d_p is comparable with w_0, because the in-plane temperature gradients become comparable with the through-plane gradients (Fig. 4b). This allows measurements of k by performing at least two TDTR measurements at different f_{mod} values[100]. An example of this type of measurement is shown for hexagonal boron nitride[104] in Fig. 4e. A standard TDTR measurement with $w_0 \gg d_p$ provides a measurement of k_z and G. Then, a second measurement where w_0 is comparable with d_p allows the value of k_r to be determined. Sensitivity to k_r is maximized when $d_p = w_0$ (ref. 105). We note that for TDTR measurements where w_0 is comparable with d_p, the predictions of the thermal model become more sensitive to w_0 than any other model parameter[70], so uncertainty in the size of the focused laser spot will cause error in the best-fit value for k_r. As noted in 'Sample preparation and choosing a transducer', it is desirable to minimize the in-plane conductance of the transducer, $k_t h_t$.

Beam-offset measurements of in-plane thermal conductivity

Beam-offset TDTR is a refinement of the conventional TDTR technique, developed by Feser and Cahill[70,71] that exploits a deliberate lateral displacement between the pump and probe beams to interrogate in-plane heat spreading. In a beam-offset measurement, the signals are measured as a function of the beam offset distance. Beam-offset measurement of InSe[106] is shown in Fig. 4f. The full width at half maximum (FWHM) of the out-of-phase signal as a function of the offset distance provides a direct measure of the thermal penetration depth in the in-plane direction ($d_{p,r}$)[71].

A key feature of beam-offset measurements is that the measured FWHM along a specific direction is nearly independent of the material's k in orthogonal directions. For example, consider beam-offset measurements of (110) quartz performed by Feser and Cahill[71]. The FWHM of the out-of-phase signal along the c axis is ≈20× as sensitive to the k of quartz along the c axis than along the a axis. Thus, this technique provides an excellent way to measure anisotropic k tensors, such as in quartz[71], ZnO[107] or black phosphorus[108,109].

The sensitivity of beam-offset measurements to k_r is maximized when $d_{p,r}$ is equal to w_0. In the limit $d_{p,r} \ll w_0$, the FWHM of the out-of-phase signal depends only on w_0, and so the measurement is not sensitive to k_r. Beam-offset measurements also do not work in the opposite limit, $d_{p,r} \gg w_0$. In this low frequency limit, the thermal dynamics approach a steady-state limit without an out-of-phase signal, analogous to SSTR experiments[110]. Therefore, in this low frequency limit, the magnitude of the thermal signals depends on k_r, but the FWHM does not[107]. In steady-state conditions, the temperature profile must be independent of the heat capacity because the energy storage term in the heat equation is zero, $C(\partial T/\partial t) = 0$. Therefore, in the low frequency limit, $d_{p,r}$ stops being a useful parameter for describing the thermal dynamics.

Heat capacity measurements

TDTR measurements performed at multiple frequencies can determine both k and C of thin films or bulk samples with low k. For thin films, one measurement uses f_{mod} such that d_p is comparable with or less than the film thickness h_f, making the result sensitive to $(kC)^n$. If $d_p < h_{film}$, then $n = 0.5$; if $d_p \geq h_{film}$, then $n < 0.5$ (ref. 111). The other measurement sets f_{mod} so that $d_p \gg h_{film}$. In this limit, sensitivity to the film's heat capacity is reduced, because most of the heat is stored in the underlying substrate (Fig. 4g). However, because the film has low k, the film remains a notable source of thermal resistance (h_{film}/k_{film}). By analysing both measurements, k_{film} and C_{film} can be simultaneously extracted such as in the case of measuring the heat capacities of ITO and FTO films[112]. This approach was also used to measure C of ultra-low-k fullerene derivatives; however, the value of C determined in this way can have large uncertainty[113], as shown in Fig. 4h.

For measurements of C for bulk materials, one measurement is conducted with $d_p \ll w_0$ to determine thermal effusivity (Eq. 2). The second measurement is performed with $d_p \sim w_0$, making the measurement sensitive primarily to thermal diffusivity (k/C). The k and C values of bulk silicon were determined with this method[114]. This approach has also been used to spatially map heat capacity in diffusion couples[115].

TR-MOKE measurements

Analysis of TDTR experiments assumes that heat is only absorbed by the transducer and that signals probe only the transducer's temperature. If the transducer is semi-transparent, one or both of these assumptions can be invalid, so generally $h_t > 50$ nm is necessary. To overcome this requirement, TR-MOKE experiments use a ferromagnetic transducer whose temperature-dependent Kerr rotation serves as a proxy for thermoreflectance[72,84]. Because changes in polarization arise only from the ferromagnetic transducer (assuming there are no other magnetic or birefringent layers in the sample stack), h_t can be a few nanometres without introducing background signals[84]. Additional details about TR-MOKE transducers are provided in Supplementary Note 3.

TR-MOKE provides superior sensitivity for frequency-dependent and beam-offset measurements of in-plane transport because it allows h_t,k_t to be minimized. In a typical TR-MOKE transducer, such as a 10 nm thick Co/Pt multilayer[116], h_t,$k_t \approx 10^{-7}$ W K^{-1}, which is 10^2 lower than for an aluminium thin film[108].

A thinner transducer also simplifies the separation of transport coefficients governing through-plane heat flow near the sample surface. For the transducer in a pump–probe experiment to cool, a region of the sample with a thickness comparable with the transducer must heat up, meaning heat must cross both the interface resistance ($1/G$) and h_t/k of thermal resistance in the sample. In TDTR measurements of a metal on an amorphous material, the latter resistance dominates and it is not possible to measure G. Using TR-MOKE with transducer thicknesses between 4 and 8 nm, the metal/amorphous-SiO_2 interface conductance was determined to be ≈300 MW m^{-2} K^{-1}, and the Si/SiO_2 interface conductance was found to be larger than 600 MW m^{-2} K^{-1} (ref. 72). Thin transducers also allow better measurements of thin films with high k values[117,118]. In TDTR measurements of high k films, the sensitivity to k of the film comes primarily from V_{out} (frequency-domain response at f_{mod}) because the time evolution of V_{in} is governed by G. Relying on sensitivity to k_{film} from V_{out} is problematic, because it requires h_{film} to be comparable with d_p, which is in the order of micrometres if k_{film} is high. TR-MOKE solves this problem by decreasing the thermal response time of the transducer to much less than 1 ns. The time evolution of the signal on nanosecond timescales can then be used to resolve k_{film}. By making h_t small and using a TiN adhesion layer to make G large, it is possible to resolve k of AlN films with $k \approx 200$ W m^{-1} K^{-1} and h_{film} between 100 and 400 nm (ref. 73) (Fig. 5a,b).

Laser-flash TDTR

A drawback of standard TDTR experiments is that they do not provide direct information about depth-dependent temperature profiles. Such information is useful for improving sensitivity to buried resistances[119], understanding non-equilibrium heat transfer by electrons[120] and accurately resolving multiple through-plane transport coefficients[75]. To address this limitation, TDTR experiments can be conducted in a laser-flash geometry. In a laser-flash TDTR experiment, instead of a single metal transducer serving the dual purpose of absorbing the pump laser (heater layer) and serving as an optical thermometer (thermometer layer), these functions are separated into different layers. Laser-flash TDTR has been used to study transport in metal multilayers[97,120,121], the thermal resistance of oxide tunnel junctions[85] and the nature of transport in amorphous thin films[75]. The combination of laser-flash TDTR and TR-MOKE enabled the first quantitative measurements of the spin-dependent Seebeck effect in ferromagnetic metals[122].

Initial laser-flash TDTR experiments gathered extra information about transport by analysing the time-domain response[123]. This limited the utility of the technique to multilayers thin enough for heat to diffuse across the structure within a few nanoseconds. Recently, a frequency-domain thermal model was developed that allows for accurate prediction of the accumulated response in a laser-flash geometry[74], enabling thicker samples to be studied[75].

In a laser-flash TDTR experiment, the in-phase signal measures the time of flight of heat across the sample, similar to the thermal response from a single pulse. Examples of TDTR measurements in a laser-flash geometry are shown in Fig. 5c,d. Data are shown for a-Si layers of different thicknesses and $k = 0.6$ W m^{-1} K^{-1}. Analogous to beam-offset measurements of $d_{p,r}$, laser-flash TDTR measurements provide a direct measure of $d_{p,z}$. This is because the phase and amplitude of the temperature response from harmonic heating is governed by z/d_p.

Applications

In this section, we highlight studies that demonstrate the versatility of TDTR in measuring thermal properties across diverse systems.

Thermal interface conductance

Interfaces are critical to nanoscale thermal transport and high thermal interface conductance is desirable for optimizing thermal management in modern electronic systems[124–128]. TDTR has refined our understanding of G[13,14,66,129–132] by making it possible to test theoretical models[123,133–135] as TDTR probes characteristic length scales comparable with the Kapitza lengths of most interfaces, $L_K = k/G$. The Kapitza length is the thickness of material that would produce the same temperature drop as the interface does.

TDTR studies have established that most metal/insulator interfaces fall in a narrow range between 40 and 400 MW m^{-2} K^{-1} (refs. 14,130,136,137). However, numerous systems are observed to have low conductance ($G < 40$ MW m^{-2} K^{-1}) due to weak bonding and/or phonon focusing[22,48,51,52,137–140]. Alternatively, numerous strongly bonded materials with high speeds of sound have high conductance ($G > 400$ MW m^{-2}–K^{-1})[96,97,126,127].

Measuring the temperature and/or pressure dependence of material properties is essential for understanding their microscopic origins. As an optical, non-contact method, TDTR can be directly applied to samples in diamond anvil cells, cryostats or high-temperature stages[96,141–146]. For example, pressure-dependent[144] and temperature-dependent[96] TDTR measurements of G have played a key part in testing theory predictions about the effect of inelastic processes on interfacial heat currents[147–158].

Thermal conductivity

High thermal conductivity materials. Understanding thermal transport mechanisms in high-k semiconductors (GaN, AlN, diamond, BN and BAs) is essential for high-performing electronics and photonics[117,118]. TDTR's micrometre-scale resolution makes it well suited for characterizing boron-based crystals, for which it is an ongoing challenge to grow large crystals that are homogeneous and have high purity[159]. Recent studies have used TDTR to probe isotropic high k in boron-based crystals, including cubic BAs[40,41,160–162], natural and isotope-enriched cubic BN[163] and BP[164,165]. Notably, TDTR enabled the thermal characterization of cubic BAs[166], a material predicted by ab initio theory to have a k value exceeding 1,000 W m^{-1} K^{-1} (refs. 167–169). When measured by TDTR, the k of isotopically enriched BAs was reported to be ≈1,500 W m^{-1} K^{-1} (ref. 161). The ability to perform TDTR on BAs within a diamond anvil cell enabled the discovery of unusual pressure independence of BAs k due to four-phonon scattering physics[160,162,170].

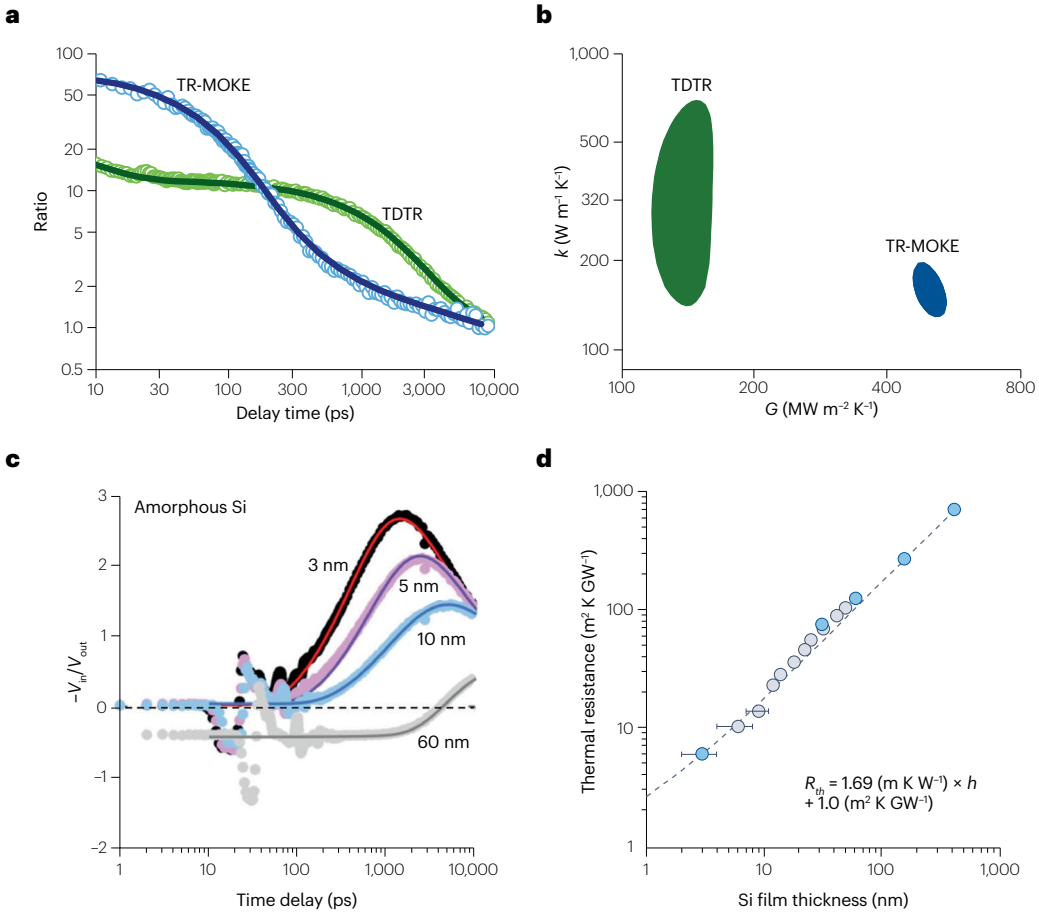

Fig. 5 | Representative data for time-resolved magneto-optic Kerr effect and laser-flash time-domain thermoreflectance. a, Thermal conductivity measurements of a 0.4 µm AlN thin film using different methods: time-resolved magneto-optic Kerr effect (TR-MOKE) with a [Pt/Co]/TiN transducer (blue circles) and time-domain thermoreflectance (TDTR) with an 80 nm Al transducer (green circles). Solid lines represent best-fit predictions from the thermal model. **b**, Contour plot showing combinations of thermal conductivity and interface conductance that yield fits to the data in panel **a** with a root-mean-square percentage error below 6.5%. TR-MOKE measurements yield a much lower uncertainty in the thermal conductivity (k) of the AlN thin film. **c**, Laser-flash TDTR data for amorphous silicon layers of different thicknesses and $k = 0.6$ W m^{-1} K^{-1}. Circles indicate experimental data and lines are the best-fit predictions by the thermal model. The ratio shows the time of flight of heat across the sample. **d**, The thermal resistance of amorphous silicon layers as a function of film thickness. Open circles indicate measurements of a wedge sample (thickness of the amorphous thin-film changes along the length of the sample) whereas filled markers indicate measurements of samples with a homogeneous film thickness. The observed linear relationship between the thermal resistance and film thickness suggests a thickness-independent thermal conductivity for amorphous silicon of 0.6 W m^{-1} K^{-1}. G, interfacial thermal conductance; R_{th}, series sum of the boundary resistance of the metal/amorphous silicon layer interface and the thermal resistance of the amorphous silicon; V_{in}, in-phase voltage signal; V_{out}, out-of-phase voltage signal. Parts **a** and **b** adapted from ref. 73, CC BY 4.0. Parts **c** and **d** adapted from ref. 75, CC BY 4.0.

Measuring k in high thermal conductivity semiconductor thin films is essential, as their conductivities are often reduced from bulk values due to phonon scattering from size effects, doping, defects and boundaries[171–173]. The submicrometre resolution of TDTR enables measurement of thin film k (refs. 173,174). However, isolating the high k value of semiconductor thin films from interfacial conductance and keeping heat confined to the film is challenging. One approach to overcome these obstacles is measuring the thermal conductivity of suspended thin films[175]. Another option is to prepare films on low thermal conductivity substrates, then choose f_{mod} and w_0 so that heat is transported in the in-plane direction[176,177]. Using a small laser spot size and low modulation frequency to confine heat within 1–10 µm thick silicon thin films on SiO_2 substrates, thermal conductivities between 100 and 150 W m^{-1} K^{-1} were measured[176]. Another method is to improve the measurement's depth resolution. For example, the ~5–10 nm ferromagnetic transducers used in TR-MOKE measurements confine heat close to the sample surface at short delay times, as discussed in 'Results'[73].

Ultra-low thermal conductivity materials. Prior to the development of TDTR, it was believed that the minimum k value of a fully dense solid was governed by the amorphous limit, as described by the Cahill–Pohl model[178]. The Cahill–Pohl model assumes that, in a disordered solid, vibrational modes will have mean free paths equal to half their wavelength. Shortly after its development, TDTR disrupted this old paradigm by identifying numerous thin films whose k value is dramatically lower than this theoretical limit[113,179,180]. For example,

TDTR was used to measure ultra-low cross-plane k in layered WSe_2 (~0.05 W m^{-1} K^{-1}), six times lower than the predicted minimum[181]. Subsequent theories suggested that a high degree of elastic anisotropy has a critical role in suppressing k in the cross-plane direction[146]. This was tested experimentally through TDTR measurements on muscovite mica by tuning its elastic anisotropy under high pressures in a diamond anvil cell[146]. Recent studies have demonstrated that ultra-low k in layered systems such as $MoSe_2$ (ref. 182), r-MoS_2 (ref. 183) and r-WS_2 (ref. 183) is closely linked to a reduction in shear modulus caused by turbostratic disorder[184]. Ultra-low cross-plane k has also been observed using TDTR in lattice-mismatched $SnSe_2(MoSe_2)_{1.32}$ heterostructures[185] and ordered intergrowths of SnSe and $MoSe_2$ isomers[186], where incommensurate stacking and structural sequencing suppress phonon transport.

Thermal anisotropy

2D materials are of interest both for probing non-classical heat transport at the nanoscale[187] and for applications in optoelectronics, biosensing and energy storage[188–190]. Resolving the thermal conductivity tensor in anisotropic materials is challenging, as it requires experimental control of the temperature fields and the ability to spatially resolve those temperature fields[105]. TDTR and its variants have been instrumental in resolving anisotropic k in 2D materials[70,105,107,108,191,192].

TDTR has several advantages for resolving anisotropy over other techniques. Unlike suspended micro-bridge and 3ω techniques, TDTR avoids complex nanofabrication. TDTR can be conducted on small flakes with dimensions in the order of ~20 μm (refs. 105,187). In comparison with Raman thermometry experiments, which are carried out under steady-state conditions, the ability to tune f_{mod} and w_0 make it easier to control temperature fields in TDTR. Raman thermometry measurements typically use the same beam to heat and to measure temperature. This precludes spatial mapping of the temperature fields along different crystal axes. Raman measurements also require modelling of the absorption versus depth, which can introduce uncertainty[187].

Beam-offset TDTR and TR-MOKE were used to measure the thermal conductivity tensor along the zigzag, armchair and through-plane directions of black phosphorus[108,109] (Fig. 6a), illustrating how structural asymmetry affects thermal anisotropy. Figure 6b shows a 2D image of the out-of-phase TR-MOKE signal, revealing in-plane anisotropy between the zigzag and armchair axes[108]. Fitting to the FWHM of the contours yielded an in-plane $k_{zigzag}/k_{armchair}$ anisotropy ratio of ~3 (ref. 108) (Fig. 6c). The through-plane conductivity was measured independently using large-spot TR-MOKE, corresponding to a $k_{zigzag}/k_{through\text{-}plane}$ anisotropy ratio of ~20 (ref. 108). The anisotropy was attributed to structural asymmetry of the puckered orthorhombic lattice, which causes direction-dependent elastic constants and phonon scattering rates.

TDTR has been used to study the in-plane and through-plane thermal conductivities of layered transition metal dichalcogenides (TMDs), including MoS_2, WS_2, $MoSe_2$ and WSe_2, revealing thermal anisotropy ratios of up to ~15 (ref. 191). Notably, the through-plane conductivity and the Al–TMD interfacial conductance showed a clear dependence on the pump modulation frequency[191]. Layered TMDs have a phonon bandgap that arises from the large mass contrast between the heavy transition metal atom and the lighter chalcogen atoms[193]. The observed dependence of k_z and the Al/TMD interfacial conductance on pump modulation frequency was credited to a non-equilibrium thermal resistance between different phonon groups within the TMDs[191].

TDTR has also been used to study the effects of structural and compositional disorder on the thermal anisotropy of MoS_2 during lithiation[194]. An increase of the thermal anisotropy ratio with lithiation in bulk Li_xMoS_2 crystals was observed, and was attributed to a combination of phonon-focusing effects caused by disorder occurring at different length scales in the in-plane and through-plane directions[194].

Additional control over temperature fields can be gained by beam shaping. A number of research groups have used non-circular heater geometries to probe in-plane anisotropic thermal conductivity[107,192,195]. Elliptical-beam TDTR uses an elliptical pump to create a quasi-2D temperature gradient[107]. Rotating the beam orientation allows directional sensitivity to in-plane conductivity[107], and was used to extract the full thermal conductivity tensor of β-Ga_2O_3 with an anisotropy ratio of ~2 between the [010] and [100] directions[195]. In a separate approach, a 1D beam-offset FDTR geometry combines a line-shaped pump with a spatially offset probe to sample the temperature field further from the heat source than is possible with Gaussian beams[192]. This method was used to measure in-plane thermal diffusivity in suspended silicon, polymers and highly ordered pyrolytic graphite[192].

Thermal property mapping

Thermal property mapping is crucial for revealing how microstructural features such as grain boundaries, defects and crystallographic anisotropy influence local heat flow in materials[17,196]. TDTR has emerged as a transformative tool for spatially resolved thermal property mapping[65,197]. Unlike electron backscatter diffraction (EBSD) and Raman thermometry, TDTR requires minimal sample preparation and allows for rapid, high-throughput imaging[19,20]. The micrometre-scale spatial resolution of TDTR mapping has allowed for thermal characterization of grain boundaries[196,198] and interface quality[199,200], as well as materials with composition distributions[15,201–203]. Pioneering work used TDTR to map k for a Nb–Ti–Cr–Si diffusion multiple, revealing anisotropic thermal conductivity in $(Ti,Nb)_3Si$ grains[65]. Thermal conductivity mapping with TDTR helps distinguish between amorphous and crystalline regions in thermally grown oxides used in aerospace coatings based on their structural-phase-dependent k[19,20].

Combining TDTR mapping with electron microscopy is a powerful method for understanding microstructure–thermal transport relationships. Thermal conductivity maps of polycrystalline diamond were correlated with EBSD imaging of the microstructure in boron-doped polycrystalline diamond (Fig. 6d) to quantify the effect of grain boundaries on transport[196]. Similarly, by correlating scanning electron microscopy backscattered electron and EBSD band contrast micrographs with thermal conductivity maps of a stabilization-annealed Si–ytterbium disilicate (YbDS) environmental barrier coating, as shown in Fig. 6e, TDTR tracked phase evolution within the coating[18]. The results demonstrated that volatilization of SiO_2 from YbDS at the surface led to the formation of ytterbium monosilicate[18].

Thermal properties of liquids and biological samples

Measuring the thermal properties of liquids is useful for a diverse array of reasons, from device thermal management[204–206] and biomedical applications[207–209] to modelling the interiors of exoplanets[210]. The most common way of measuring k of liquids is the hot-wire method, which is based on electrical heating and temperature sensing of a submerged metal wire. TDTR offers advantages over this approach by requiring only a few microlitres of fluid, which eliminates convection effects. TDTR also has advantages over transient grating methods because it is insensitive to the liquid's optical properties[45]. Figure 6f shows an example of

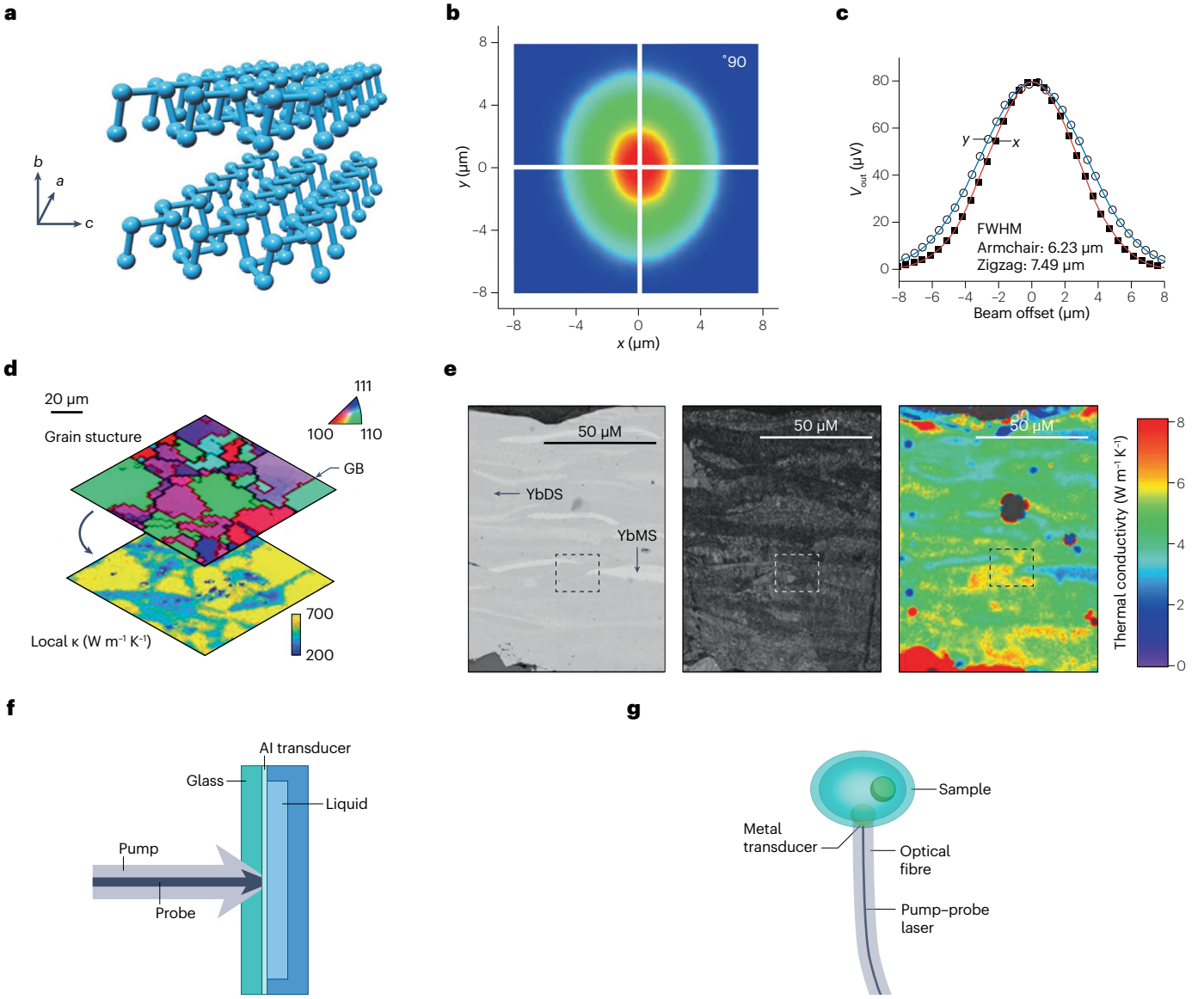

Fig. 6 | Diverse applications of time-domain thermoreflectance for thermal characterization. a, Lattice structure of black phosphorus. Coordinates *a*, *b* and *c* correspond to the in-plane zigzag, through-plane and in-plane armchair directions, respectively. **b**, In-plane beam-offset contour measured at 90° of sample-loading orientation with a 20× objective lens and a 1.6 MHz laser modulation frequency to facilitate the in-plane thermal transport. **c**, Beam-offset signal extracted from panel **a** along the *x* (squares) and *y* (circles) directions, with blue and red lines showing the corresponding thermal model fits. **d**, Correlative electron backscatter diffraction (EBSD)–time-domain thermoreflectance (TDTR) microscopy of polycrystalline diamond, where the colour segment indicates the local crystal orientation relative to the *x* axis. **e**, Scanning electron microscopy backscattered electron and EBSD band contrast micrographs of a stabilization-annealed specimen with the corresponding thermal conductivity micrograph, with red and yellow regions representative of ytterbium disilicate (YbDS) and ytterbium monosilicate (YbMS), respectively. **f**, TDTR can be used to measure the thermal properties of liquids. **g**, Fibre-based thermoreflectance sensor that guides pump and probe beams through an optical fibre. GB, grain boundary. FWHM, full width at half maximum; V_{out}, out-of-phase voltage signal. Parts **a**–**c** adapted with permission from ref. 108, Wiley. Part **d** adapted with permission from ref. 196, American Chemical Society. Part **e** adapted with permission from ref. 18, Elsevier. Part **f** adapted with permission from ref. 45, American Institute of Physics. Part **g** adapted with permission from ref. 207, American Institute of Physics.

how TDTR can be used to measure the thermal properties of liquids and liquid–solid interfaces[45]. TDTR was used to measure the thermal conductivity of water–methanol mixtures, revealing that the addition of methanol reduces the thermal conductivity compared with pure water, with values 10% lower than the 0.55 W m^{-1} K^{-1} measured for pure water[210].

The interfacial conductance between water and hydrophilic versus hydrophobic surfaces has also been measured by TDTR, helping establish the maximum vapour layer thickness at hydrophobic interfaces[209]. TDTR has enabled the characterization of local heat transfer coefficients in electronic device hot spots cooled by microchannels[205],

jet impingement[204] and two-phase cooling[206], and the thermal dynamics of water droplets that interact with hot surfaces[211,212]. A high-speed oscilloscope connected to the lock-in amplifier was used to measure transient changes in the TDTR ratio during the single-bubble ebullition cycle in a microchannel[206], identifying microlayer evaporation as the dominant heat transfer mechanism and offering key insight into phase-change cooling[206].

A related but distinct application of TDTR is measurement of biological samples, as the sample geometry is similar to that of liquids. TDTR offers key advantages over electrical methods for biological applications by using non-contact heating and temperature sensing[207]. This eliminates challenges related to fabrication and integration, making TDTR better suited for complex or delicate sample environments[207]. The use of a fibre-based thermoreflectance sensor that guides pump and probe beams through an optical fibre (Fig. 6g) enables in situ TDTR measurements on biological samples with challenging geometries[207]. This configuration allows accurate thermal measurements of liquids and biomaterials available in small volumes or located in hard-to-reach regions and has been used to determine the thermal effusivity of diverse biological and agricultural samples, from butter to pork liver[207].

Thermal property measurements with external stimuli

Studying thermal transport in materials whose thermal properties change under external stimuli, such as electric fields, carrier concentration, chemical intercalation, mechanical strain or magnetic fields, is critical for improving technologies that require precise heat control at small length scales. These technologies include thermal diodes[46], transistors[199] and switches[213], as well as thin, flexible electronic devices[214] and spin-based systems[215]. Additionally, thermal measurements under high-pressure conditions are essential for geophysical modelling, as pressure-dependent k influences heat flow predictions for planetary interiors[216].

TDTR is well suited for time-resolved measurements of the electric field effects on different material systems, such as electrochemical intercalation[199] and electric field-driven domain switching[46]. Applying an electric field to suspended PZT membranes drives ferroelastic domain wall motion on nanosecond timescales[46]. TDTR was used to measure the resulting change in k, observing a reversible 13% increase associated with reduced domain wall density[46]. Not only can TDTR be used to measure thermal conductance during electrochemical cycling but it can also spatially map its evolution in real time across a working device, as shown by in situ measurements on ultrathin MoS_2 during lithium intercalation[199].

The capability to apply magnetic fields during TDTR measurements expands its applicability to systems where thermal transport is affected by field-responsive molecular alignment[213] or magneto-structural coupling[215]. One such system is a magnetically responsive liquid crystal network, in which mesogenic units align anisotropically under a magnetic field and affect the direction of heat flow[213]. TDTR performed under magnetic fields at elevated temperatures allowed direct, in situ measurement of changes in k resulting from this reorientation[213].

Thermal characterization of ion-irradiated materials

TDTR has become a key non-contact, non-destructive technique for studying the impact of ion irradiation on the thermal properties of materials, with applications ranging from semiconductor devices to nuclear reactors[217–219]. Ion irradiation produces a subsurface micrometre-scale damage layer which is inaccessible to direct-contact probes[220]. By varying the thermal penetration depth, TDTR enables non-destructive depth profiling of k within the irradiated region[220].

The thermal properties of semiconductors exposed to ion irradiation are important for cooling electronic devices[219]. TDTR has been used to examine the effect of Ga^+ focused ion beam processing on silicon, revealing a reduction in k due to the formation of amorphous regions and structural disorder[219].

TDTR has been used to characterize and identify novel materials for nuclear applications[218], and to quantify radiation-induced thermal degradation in materials relevant to nuclear energy systems[217]. Ion irradiation replicates neutron-induced displacement damage and TDTR measurements of tetragonal lithium aluminate (γ-$LiAlO_2$) have shown that irradiation reduces k by up to 90%, reaching values near 1 $W\,m^{-1}\,K^{-1}$ at high fluence[217].

Thermal characterization of ion-irradiated materials offers a controlled means to investigate phonon scattering and the mechanisms that govern thermal transport in disordered systems[220–223]. For example, TDTR measurements of k in irradiated silicon showed that a reduction in k due to ion irradiation can be reversed by annealing[222]. This indicates that structural disorder from ion-induced damage and boundary scattering reduces k more effectively than impurity scattering from the ions themselves[219,220,222]. In amorphous carbon films, ion irradiation has been shown to anomalously enhance k with increasing ion fluence and energy[224]. This enhancement results from stiffening, densification and increased carbon network connectivity[224]. Finally, TDTR has been used to show how ion-induced point defects, near-surface disorder, bond breaking and surface roughness influence interface thermal conductance[225–228].

Reproducibility and data deposition

If samples are stable during the TDTR scan — for example, there is no structural/chemical evolution as a function of time or temperature or any other external stimulus — independent measurements on a sample typically differ by less than a few per cent. As a result, most TDTR errors are systematic, arising from uncertainties in model parameters, experimental designs that do not account for coupled parameters or spurious signals. In the following sections, we discuss how to manage and quantify these systematic errors, address the importance of accurately determining beam spot size, identify and mitigate spurious signals, and examine the main noise sources in TDTR.

Error analysis

In TDTR experiments, k can be determined with 5–10% uncertainty, but complexities such as thin films or multiple unknown parameters increase measurement errors. For accurate TDTR experiments, typically only two independent parameters should be fit per dataset. All other model parameters need to be accurately known. To estimate uncertainties, parametric sensitivity analysis or Monte Carlo methods are useful tools. Both of these approaches are expounded further upon in the Supplementary Note 4.

Spot size uncertainty

Determining the spot size is important for accurately modelling the TDTR signal. There are several ways to determine spot sizes. The first method involves analysing the Gaussian intensity of the V_{in} signal using a beam-offset scan at high modulation frequencies at a delay time of approximately +100 ps. Also, imaging the pump and probe beams with the integrated camera and then analysing the resulting beam profile

in image analyses software, such as ImageJ, will help obtain the spot size within 5% uncertainty. Lastly, performing a concentric TDTR measurement where $d_p \sim w_0$ on a high-k substrate will also yield an independent measurement of spot size. As high thermal conductivity insulators display mean free path effects, high-purity single-crystal metals work best for this method (namely aluminium or copper).

Spurious signals

Spurious signals in TDTR experiments lead to systematic errors by adding unwanted voltage contributions that deviate from the predicted thermal response. Spurious signals should not be confused with noise, as noise can be removed by averaging. Spurious signals are real signals at f_{mod} that are detected by the lock-in but are not related to the sample's thermoreflectance signals. Common sources include coupling between the circuit driving the electro-optic modulator and the detection circuit, coherent pickup by the radio-frequency lock-in, partial beam clipping or misalignment in the optical set-up, thermoelastic effects in soft materials and partial transparency of the metal transducer. A number of steps can be taken to avoid spurious signals, such as measuring the specular reflectance, optical chopping, using double-shielded coaxial cables, carefully maintaining beam alignment and monitoring absolute signals (V_{in}, V_{out}) to diagnose alignment issues. Rough sample surfaces can also cause spurious signals, as explained in Supplementary Note 5.

Noise

In TDTR experiments, noise typically stems from three primary sources: electronic noise; intensity noise from the laser; and noise from fluctuations in the amplitude of the electro-optic modulator modulation. The detection circuit should be designed such that the laser intensity noise dominates over the electronics noise. The laser intensity noise follows a $1/f_{mod}$ dependence at modulation frequencies below 1 MHz (ref. 229). At frequencies near 10 MHz, the intensity noise in a Ti:sapphire laser approaches the shot-noise limit. To mitigate the effects of laser intensity fluctuations at lower frequencies, balanced detection can be used, as shown in Supplementary Fig. 1.

Limitations and optimizations

TDTR is a powerful technique, but has numerous limitations. Owing to intensity noise and pulse accumulation in the in-phase signal (Supplementary Note 5), TDTR measurements are rarely performed at $f_{mod} < 0.1$ MHz. This has drawbacks, such as limiting the ability of TDTR to probe buried interfaces. In Supplementary Note 2, we suggest methods for overcoming this limitation. In low-k samples, such as polymers, the high modulation frequencies of TDTR ($f_{mod} > 0.1$ MHz) mean that a small region within 100–200 nm of the surface is measured. This is not ideal for bulk samples where the surface microstructure may or may not be representative of the bulk interior. TDTR does not work for rough samples, which is discussed in greater detail in Supplementary Note 5. TDTR struggles with measurements at very high (>900 K) and very low (<30 K) temperatures. At high temperatures, the transducer tends to fail[96,230], whereas at low temperatures small heat capacities make per-pulse temperature rises large compared with the ambient temperature[129,231]. As a result, thermal properties fluctuate with the temperature. The standard analytical approach for analysing TDTR signals cannot accommodate this. Another drawback of TDTR is that accurate knowledge of heat capacities is required, which can be unknown in novel material systems.

Mean free path effects

When critical length scales, such as d_p, approach phonon mean free paths (ℓ), the heat diffusion equation becomes inaccurate. As a result, TDTR cannot measure k of non-metallic crystals at low temperatures[232], or with sub-micrometre w_0 at room temperature[231]. The heat diffusion equation predicts that the heat current scales with $\Delta T/d_p$, where ΔT describes the excess surface temperature of the sample caused by heating. Therefore, the heat diffusion equation predicts that ΔT continually decreases with increasing f_{mod} due to ever-increasing temperature gradients. In reality, when d_p approaches ℓ, transport is expected to reach a ballistic limit where the heat current is proportional to ΔT. Consequently, analysing TDTR data with the heat diffusion equation leads to best-fit values for k (sometimes called apparent values) that are low[233,234]. Reducing w_0 to be lower than ℓ can induce similar ballistic effects[232]. Frequency-dependent deviations from Fourier's predictions are easiest to observe in alloys with point-defect scattering[233]. By contrast, spot size-dependent deviations are most often observed in single crystals[235].

Over the past 15 years, numerous theoretical studies have clarified the physics underlying these experimental measurements. Trends with f_{mod} have been explained both in terms of super-diffusive transport[236,237] and by emphasizing the importance of interfaces, suggesting thermal resistance from interfacial scattering extends over length scales comparable with mean free paths[88,231]. Importantly, this thermal resistance is not induced solely by high heating frequency; instead, high heating frequency increases the measurement's sensitivity to this effect. Recent theoretical studies support this interpretation[238–240]. The importance of interfacial scattering in TDTR measurements of silicon demonstrated that the relatively small frequency-dependent deviations from predictions of the heat diffusion equation can be explained by considering the dependence of interfacial phonon scattering rates on phonon frequency[241].

The complex interplay of interfacial scattering and ballistic transport in TDTR experiments offer opportunities for discovery. We believe further progress requires improved spatio-temporal resolution of the temperature profile, such as the kind offered by TR-MOKE and laser-flash experiments. Another important open question is why SSTR measurements, unlike TDTR measurements, are in agreement with diffusive predictions at low temperatures[242], even when mean free paths exceed the spot size. More work in this space will elucidate the important interplay among different thermometry techniques rooted in impulse, periodic and/or steady-state heating conditions with combinations of in-phase and out-of-phase temperature responses on the ability to resolve intrinsic thermal conductivities of crystals and quasi-ballistic heat transport.

Measuring thermal conductivity without volumetric heat capacity

Modelling of the thermal response of the sample in a TDTR experiment requires knowledge of the sample's heat capacity. It is sometimes possible to measure heat capacity (as discussed in 'Results'), but not always. For example, heat capacity of a thin film cannot be measured if $h_{film} < d_p$, or in complex heterostructures. Therefore, a direct measure of k is desirable. Braun et al. developed SSTR, a pump–probe technique utilizing two continuous wave lasers where the pump beam is modulated at low enough frequencies that the sample reaches steady-state conditions during the on time of the pump[110]. In this approach, the thermoreflectance is monitored as a function of pump power and compared with a reference standard, which in this

Glossary

Coherent pickup
Unintended leakage of the reference signal at the pump modulation frequency (f_{mod}) into the measurement input of the lock-in through radiative, capacitive or conduction paths. As it occurs at the reference frequency, it cannot be filtered out by the lock-in, despite not originating from the sample.

Mean free paths
The average distances that particles or quasi-particles (carriers such as electrons, phonons or magnons) travel between scattering events that alter their momentum or energy.

Multilayer thermal model
A framework for predicting the thermal response of the sample to heating. Thermal transport in each layer is assumed to be governed by a layer-specific heat equation, and transport between layers is governed by boundary conditions that assume the heat current is continuous across the boundary and that temperature drops at the interface are governed by the interface conductance between the two layers.

Phonon focusing
The propagation of phonons preferentially along certain crystallographic orientations in anisotropic materials.

Picosecond acoustics
Non-thermal signals in pump–probe measurements that arise from strain-induced changes to the reflectivity. The initial temperature gradient in the metal transducer after absorption of the pump pulse generates a strain wave that propagates into the sample, reflects from buried interfaces and eventually returns to the metal film surface. The time delay of the acoustic waves' echoes is determined by the film thickness and the longitudinal speed of sound.

Pulse accumulation
Temperature response of the sample caused by the accumulated response from the pump pulses that heated the sample prior to zero time delay. Pulse accumulation occurs when energy from a previous pulse is not conducted away before the arrival of the subsequent pump pulse.

Thermal model
The iterative Feldman algorithm used to analyse heat conduction in layered structures.

Thermal transport phenomena
The processes involved in the transfer of energy (heat) through various media, including solids, liquids and gases.

Thermoreflectance
Change of reflectance with temperature.

steady-state regime becomes a measure of the k of the sample without sensitivity to the material's heat capacity. Thus, SSTR offers a method to measure k, which has been validated on measurements of thermal conductivity on low thermal conductivity materials such as [6,6]-phenyl-C_{61}-butyric acid methyl ester (PCBM)[180] and high thermal conductivity materials such as diamond[110]. SSTR has also been used to measure the thermal resistance of thin films and device-relevant heterostructures on length scales overlapping with those of TDTR, providing a complementary path forward for thermal measurements[112,243]. Additionally, SSTR and TDTR used in tandem have recently demonstrated the utility to reduce the uncertainty in determining the thermal properties of thin films and interfaces[174,180,242,244,245]. Thus, in addition to SSTR providing measurement of k without knowledge of heat capacity, these combinations of SSTR with TDTR and their related techniques offer new opportunities for nanoscale thermometry[246].

Probing deeper into samples

The thermal penetration depth in TDTR is usually limited by the relatively high modulation frequency (usually ranging from a few 100 nm to a few micrometres, depending on the k of the sample)[7]. This limiting sample volume calls into question the applicability of TDTR to provide a sufficient representation of the thermal properties of materials with characteristic thicknesses that are in the order of tens of micrometres or greater. Although this relatively shallow sampling volume in TDTR should not pose a problem in high-quality, homogeneous materials (such as monolithic wafers), the limitation in TDTR is apparent for material systems with larger length-scale heterogeneous distributions of phases, defects or interfaces where the micrometre-scale measurement volume of TDTR would not provide a representation of the entire sample. Additionally, the ability to systematically control this depth sampling volume during proper thermal measurements would allow for detecting subsurface thermal resistances[100,247], including creating thermal conductivity depth profiles, an approach with TDTR measurements that has only recently been demonstrated[220], still within the relatively shallow subsurface depth of measurement typical in TDTR. Laser-flash TDTR offers a TDTR variant to measure larger volumes than a typical single-sided TDTR measurement, but continuous wave-based pump–probe thermoreflectance alternatives also offer this increased depth sensitivity, discussed below.

The reasonably measurable upper limit of the thermal penetration depth during typical single-sided pump–probe experiments is in the order of the pump spot size[7,248], which can be accessed in the steady-state limit. Thus, SSTR offers an opportunity to thermally probe under a sample surface as compared with typical implementations of TDTR as the thermal gradients induced during an SSTR experiment reach depths in the order of the spot size[249]; this has recently been demonstrated to detect the thermal resistance of buried substrates, interfaces and damaged layers[245,250,251]. The thermal penetration depth could then be varied to sample different volumes by varying the spot size in SSTR, or through the use of FDTR.

Although frequency-domain modulation in continuous wave, laser-based pump–probe methods has been implemented for four decades[57,58,252], more recently Schmidt et al.[253]. embraced commonalities in hardware, detection and thermal analysis from TDTR that have enabled FDTR to extend to much higher frequencies and broadband modulation[254–259]. By making FDTR measurements over wide ranges of frequencies, the thermal penetration depth is continuously varied up to the upper limit of the spot size, and thus thermal conductivity depth profiles are feasible[260,261]. Additionally, with larger spot sizes, the FDTR thermal penetration depth can be increased at lower frequencies, thus enabling thermal property measurements of subsurface films and interfaces at depths deeper than those accessed by TDTR[262–265].

It should be noted that in the low frequency limit, TDTR and FDTR essentially become SSTR, and thus there are opportunities for single thermometry platforms to perform both FDTR and SSTR measurements. This allows for accurate thermal resistance measurements of multiple films and interfaces with reduced uncertainty as compared with a single technique alone. This tandem approach, coupled with machine learning algorithms, can enable resolution to additional thermal property information with lower uncertainties than previously realized[260,261], offering a unique outlook for artificial intelligence machine learning-driven thermometry inspired by TDTR, FDTR and SSTR.

Outlook

Since the advances in pump–probe experimentation provided by Cahill, which have given rise to the now nearly standardized TDTR configuration

detailed in this Primer, TDTR and its offshoots continue to be the most widely used thermometry platforms for determining k of thin films and bulk materials along with thermal interface conductance across material interfaces. The continued societal focus and growth of critical technologies that underpin next-generation computing, modern memory technologies, data centres powering artificial intelligence, energy storage for electric transportation and communication or radar are all reliant on lower dimensionality materials and devices that have the requisite thermal transport properties to handle the immense power dissipation demands. TDTR will thus continue to be a staple in thermometry to ensure these requisite material thermal transport properties.

As TDTR has inspired evolutions to overcome its various limitations, opportunities exist to continue to advance thermometry through combining the principles of TDTR with other established experimental methods to advance nanoscale thermometry in different directions and towards new extremes. For example, although most common optical spectroscopy platforms interrogate the optical response of materials across ranges of photon wavelengths to understand the electronic, phononic, chemical and physical structure of materials, TDTR interrogates the time-domain and frequency-domain thermal response of materials using only a single wavelength or a relatively narrow spectrum of wavelengths encapsulated by the spectral bandwidth of the laser pulse (~10–12 nm). Expanding TDTR to include a broad spectrum of UV, visible and/or infrared pump and probe wavelengths will enable its future applicability to wider arrays of materials, including the possibility of using TDTR directly on non-metals without the use of a transducer by exciting electrons above the bandgap[89,266] or absorbing directly with optical phonon modes[267–269]. The challenge here, however, lies in harnessing this broad-spectrum photon tuning while still generating an out-of-phase response, which would require higher repetition rate laser systems with sufficient pulse energy for broad-spectrum photon conversion.

Although TDTR has proven exceptional cross-plane spatial resolution in thermal resistance measurements, the lateral resolution is ultimately limited by the diffraction-limited spot size. Other classes of optical and thermal metrologies achieve true-nanoscale lateral resolution through near-field focusing techniques or scanning probe methods (such as scanning thermal microscopy)[270,271], respectively. A low barrier to entry for extending the resolution of TDTR to sub-diffraction limit areal resolution could involve patterning transducers with sub-diffraction limit features or using nanoparticles on the surface to achieve this same effect[272–274]. However, an approach more broadly applicable to wider classes of materials would be to combine TDTR with scanning probe methods. There has been immense progress in using optical sources combined with AFM probe tips to interrogate the properties of materials, such as tip-enhanced Raman spectroscopy[275], scanning near-field optical microscopy[268,276] and nano-FTIR[268], but the combination of AFM probes to spatially localize a pump–probe thermoreflectance measurement to length scales beyond the diffraction limit has only recently been explored[277]. This would offer unprecedented nanoscale resolution in TDTR and related techniques. However, as with several of these previous scanning probe-based thermometry techniques, the thermal contact resistance (due to water and carbon adsorption, for example) and additional near-field radiative heat transfer between the tip and the sample surface must be considered for an accurate measure of the nanoscale thermal properties of the sample[271,278]. Further, localizing the absorption of the ultrafast pump pulse will result in large thermal expansion that can lead to spurious elastic signals, making it difficult to isolate the temperature changes needed to extract the thermal properties of the substrate. Even with these considerations overcome, the thermal diffusion length scales emanating from the AFM tip heating into the sample must be carefully understood. For example, as discussed above in 'Limitations and optimizations', the upper limit of the thermal penetration depth in typical pump–probe experiments is in the order of the spot size, so although heating from an AFM tip will certainly increase spatial resolution compared with typical TDTR implementations, the mechanical deformation induced on the sample surface resulting from AFM tip penetration could lead to changes in the thermal gradients not predicted from surface heating alone, resulting in unanticipated anisotropic temperature profiles and reduced spatial resolution. Further, these sub-micrometre confined heater length scales could also lead to mean free path effects.

Finally, as we discussed in 'Applications', the non-contact nature of TDTR lends itself to provide powerful probes of heat transfer in materials being exposed to extreme environments and when external stimuli are applied to materials and basic devices. Most approaches to date rely on designing materials or simple devices that are amenable to the standard TDTR experimental configurations to study these effects. With different optical path hardware and detection designs, TDTR measurements can be extended to wider arrays of devices and environments to study thermal property changes of materials and devices in operando or even in situ during material growth or material processing. The advent of fibre optic-based pump–probe designs will facilitate this advance[279,280], which could enable real-time monitoring of device health in systems, evaluation of defect formation in materials subjected to extreme environments[281,282] or even sensors of material quality during growth that, when coupled with advanced controls and machine-learned algorithms, could provide major advances in high-throughput growth of materials with desired optical, electrical and thermal functionalities. Clearly, the future outlook of possibilities for TDTR when coupled with additional hardware and software designs and advances paints an exciting future for optimization of materials, devices and systems with length scales from the atom to application.

Published online: 28 August 2025

References

1. Cahill, D. G. Analysis of heat flow in layered structures for time-domain thermoreflectance. *Rev. Sci. Instrum.* **75**, 5119–5122 (2004).
   This work presents an introduction to and a description of the now-standardized TDTR experimental layout and data analysis, including out-of-phase signals.
2. Cahill, D. G., Goodson, K. & Majumdar, A. Thermometry and thermal transport in micro/nanoscale solid-state devices and structures. *J. Heat. Transf.* **124**, 223–241 (2002).
3. Rosei, R. & Lynch, D. W. Thermomodulation spectra of Al, Au, and Cu. *Phys. Rev. B* **5**, 3883–3894 (1972).
4. Rosei, R. Temperature modulation of the optical transitions involving the Fermi surface in Ag: theory. *Phys. Rev. B* **10**, 474–483 (1974).
5. Weaver, J. H., Lynch, D. W., Culp, C. H. & Rosei, R. Thermoreflectance of V, Nb, and paramagnetic Cr. *Phys. Rev. B* **14**, 459–463 (1976).
6. Colavita, E., Franciosi, A., Mariani, C. & Rosei, R. Thermoreflectance test of W, Mo and paramagnetic Cr band structures. *Phys. Rev. B* **27**, 4684–4693 (1983).
7. Braun, J. L. & Hopkins, P. E. Upper limit to the thermal penetration depth during modulated heating of multilayer thin films with pulsed and continuous wave lasers: a numerical study. *J. Appl. Phys.* **121**, 175107 (2017).
8. Chen, G. *Nanoscale Energy Transport and Conversion: A Parallel Treatment of Electrons, Molecules, Phonons, and Photons* (Oxford Univ. Press, 2005).
9. Zhang, Z. *Nano/Microscale Heat Transfer* (McGraw-Hill, 2007).
10. Kaviany, M. *Heat Transfer Physics* (Cambridge Univ. Press, 2008).
11. Srivastava, G. P. *The Physics of Phonons* (Taylor and Francis, 1990).
12. Swartz, E. T. & Pohl, R. O. Thermal boundary resistance. *Rev. Mod. Phys.* **61**, 605–668 (1989).
13. Hopkins, P. E. Thermal transport across solid interfaces with nanoscale imperfections: effects of roughness, disorder, dislocations, and bonding on thermal boundary conductance. *ISRN Mech. Eng.* **2013**, 1–19 (2013).

14. Monachon, C., Weber, L. & Dames, C. Thermal boundary conductance: a materials science perspective. *Annu. Rev. Mater. Res.* **46**, 433 (2016).
15. López-Honorato, E. et al. Thermal conductivity mapping of pyrolytic carbon and silicon carbide coatings on simulated fuel particles by time-domain thermoreflectance. *J. Nucl. Mater.* **378**, 35–39 (2008).
16. Zhao, J.-C., Zheng, X. & Cahill, D. G. High-throughput diffusion multiples. *Mater. Today* **8**, 28–37 (2005).
This work demonstrates using TDTR to spatially map the thermal conductivity of materials.
17. Olson, D. H. et al. Anisotropic thermal conductivity tensor of β-$Y_2Si_2O_7$ for orientational control of heat flow on micrometer scales. *Acta Mater.* **189**, 299–305 (2020).
18. Olson, D. H. et al. Evolution of microstructure and thermal conductivity of multifunctional environmental barrier coating systems. *Mater. Today Phys.* **17**, 100304 (2021).
19. Olson, D. H. et al. Local thermal conductivity measurements to determine the fraction of α-cristobalite in thermally grown oxides for aerospace applications. *Scr. Mater.* **177**, 214–217 (2020).
20. Milich, M. et al. Quantifying devitrification and porosity in thermally grown oxides through spatially-resolved time-domain thermoreflectance. *Acta Mater.* **288**, 120802 (2025).
21. Ardrey, K. D. et al. Opportunities for novel refractory alloy thermal/environmental barrier coatings using multicomponent rare earth oxides. *Scr. Mater.* **251**, 116206 (2024).
22. Koh, Y. K., Bae, M.-H., Cahill, D. G. & Pop, E. Heat conduction across monolayer and few-layer graphenes. *Nano Lett.* **10**, 4363–4368 (2010).
23. Liu, H. et al. Spontaneous chemical functionalization via coordination of Au single atoms on monolayer MoS_2. *Sci. Adv.* **6**, eabc9308 (2020).
24. Zhang, F. et al. Monolayer vanadium-doped tungsten disulfide: a room-temperature dilute magnetic semiconductor. *Adv. Sci.* **7**, 2001174 (2020).
25. Evans, A. M. et al. Thermally conductive ultra-low-*k* dielectric layers based on two-dimensional covalent organic frameworks. *Nat. Mater.* **20**, 1142–1148 (2021).
26. Cancellieri, C. et al. Interface and layer periodicity effects on the thermal conductivity of copper-based nanomultilayers with tungsten, tantalum, and tantalum nitride diffusion barriers. *J. Appl. Phys.* **128**, 195302 (2020).
27. Cheaito, R. et al. Interplay between total thickness and period thickness in the phonon thermal conductivity of superlattices from the nanoscale to the microscale: coherent versus incoherent phonon transport. *Phys. Rev. B* **97**, 085306 (2018).
28. Lorenzin, G. et al. Tensile and compressive stresses in Cu/W multilayers: correlation with microstructure, thermal stability, and thermal conductivity. *Acta Mater.* **240**, 118315 (2022).
29. Ravichandran, J. et al. Crossover from incoherent to coherent phonon scattering in epitaxial oxide superlattices. *Nat. Mater.* **13**, 168–172 (2014).
This work discusses the implications of coherent phonon transport on the thermal conductivity of superlattices determined with TDTR.
30. Chen, P. et al. Role of surface-segregation-driven intermixing on the thermal transport through planar Si/Ge superlattices. *Phys. Rev. Lett.* **111**, 115901 (2013).
31. Koh, Y. K., Cao, Y., Cahill, D. G. & Jena, D. Heat-transport mechanisms in superlattices. *Adv. Funct. Mater.* **19**, 610–615 (2009).
32. Rawat, V., Koh, Y. K., Cahill, D. G. & Sands, T. D. Thermal conductivity of (Zr,W)N/ScN metal/semiconductor multilayers and superlattices. *J. Appl. Phys.* **105**, 024909 (2009).
33. Babaei, H. et al. Observation of reduced thermal conductivity in a metal–organic framework due to the presence of adsorbates. *Nat. Commun.* **11**, 4010 (2020).
34. Erickson, K. J. et al. Thin film thermoelectric metal–organic framework with high Seebeck coefficient and low thermal conductivity. *Adv. Mat.* **27**, 3453–3459 (2015).
35. DeCoster, M. E. et al. Hybridization from guest–host interactions reduces the thermal conductivity of metal–organic frameworks. *J. Am. Chem. Soc.* **144**, 3603–3613 (2022).
36. Meirzadeh, E. et al. A few-layer covalent network of fullerenes. *Nature* **613**, 71–76 (2023).
37. Hoque, M. S. B. et al. Ruddlesden–Popper chalcogenides push the limit of mechanical stiffness and glass-like thermal conductivity in crystals. *Nat. Commun.* **16**, 6104 (2025).
38. Zhao, B. et al. Orientation-controlled anisotropy in single crystals of quasi-1D $BaTiS_3$. *Chem. Mater.* **34**, 5680–5689 (2022).
39. Dames, C. Ultrahigh thermal conductivity confirmed in boron arsenide. *Science* **361**, 549–550 (2018).
40. Kang, J. S., Li, M., Wu, H., Nguyen, H. & Hu, Y. Experimental observation of high thermal conductivity in boron arsenide. *Science* **361**, 575–578 (2018).
41. Tian, F. et al. Unusual high thermal conductivity in boron arsenide bulk crystals. *Science* **361**, 582–585 (2018).
42. Wang, X., Ho, V., Segalman, R. A. & Cahill, D. G. Thermal conductivity of high-modulus polymer fibers. *Macromolecules* **46**, 4937–4943 (2013).
43. Cahill, D. G. Extremes of heat conduction—pushing the boundaries of the thermal conductivity of materials. *MRS Bull.* **37**, 855–863 (2012).
44. Cahill, D. G. Thermal-conductivity measurement by time-domain thermoreflectance. *MRS Bull.* **43**, 782–789 (2018).
45. Schmidt, A., Chiesa, M., Chen, X. & Chen, G. An optical pump–probe technique for measuring the thermal conductivity of liquids. *Rev. Sci. Instrum.* **79**, 64902 (2008).
46. Foley, B. M. et al. Voltage-controlled bistable thermal conductivity in suspended ferroelectric thin-film membranes. *ACS Appl. Mater. Interfaces* **10**, 25493–25501 (2018).
47. Ihlefeld, J. F. et al. Room-temperature voltage tunable phonon thermal conductivity via reconfigurable interfaces in ferroelectric thin films. *Nano Lett.* **15**, 1791–1795 (2015).
This work uses TDTR to measure the thermal conductivity of a ferroelectric thin film while an electric field is applied to modulate the thermal conductivity via ferroelastic domain wall switching.
48. Foley, B. M. et al. Modifying surface energy of graphene via plasma-based chemical functionalization to tune thermal and electrical transport at metal interfaces. *Nano Lett.* **15**, 4876–4882 (2015).
49. Hopkins, P. E. et al. Measuring the thermal conductivity of porous, transparent SiO_2 films with time domain thermoreflectance. *J. Heat. Transf.* **133**, 61601 (2011).
50. Hopkins, P. E., Kaehr, B., Piekos, E. S., Dunphy, D. & Brinker, C. J. Minimum thermal conductivity considerations in aerogel thin films. *J. Appl. Phys.* **111**, 113532 (2012).
51. Rosul, M. G. et al. Thermionic transport across gold-graphene-WSe_2 van der Waals heterostructures. *Sci. Adv.* **5**, eaax7827 (2019).
52. Koh, Y. K. et al. Role of remote interfacial phonon (RIP) scattering in heat transport across graphene/SiO_2 interfaces. *Nano Lett.* **16**, 6014–6020 (2016).
53. Cho, J. et al. Electrochemically tunable thermal conductivity of lithium cobalt oxide. *Nat. Commun.* **5**, 4035 (2014).
This work uses TDTR to measure the thermal conductivity of a cathode material while an electric field is applied to modulate the thermal conductivity via lithiation.
54. Eesley, G. L. Observation of nonequilibrium electron heating in copper. *Phys. Rev. Lett.* **51**, 2140–2143 (1983).
To our knowledge, this work presents the first demonstration of using pulsed lasers (~12 ps pulse width) in a transient thermoreflectance configuration to measure thermal properties of a material.
55. Eesley, G. L. Generation of nonequlibrium electron and lattice temperatures in copper by picosecond laser pulses. *Phys. Rev. B* **33**, 2144–2151 (1986).
56. Paddock, C. A. & Eesley, G. L. Transient thermoreflectance from thin metal films. *J. Appl. Phys.* **60**, 285–290 (1986).
57. Opsal, J., Rosencwaig, A. & Willenborg, D. L. Thermal-wave detection and thin-film thickness measurements with laser beam deflection. *Appl. Opt.* **22**, 3169–3176 (1983).
58. Opsal, J. & Rosencwaig, A. Thermal and plasma wave depth profiling in silicon. *Appl. Phys. Lett.* **47**, 498–500 (1985).
59. Thomsen, C. et al. Coherent phonon generation and detection by picosecond light pulses. *Phys. Rev. Lett.* **53**, 989–992 (1984).
60. Stoner, R. J. & Maris, H. J. Kapitza conductance and heat flow between solids at temperatures from 50 to 300 K. *Phys. Rev. B* **48**, 16373–16387 (1993).
61. Bonello, B., Perrin, B. & Rossignol, C. Photothermal properties of bulk and layered materials by the picosecond acoustics technique. *J. Appl. Phys.* **83**, 3081–3088 (1998).
62. Capinski, W. S. & Maris, H. J. Improved apparatus for picosecond pump-and-probe optical measurements. *Rev. Sci. Instrum.* **67**, 2720–2726 (1996).
63. Capinski, W. S. & Maris, H. J. Thermal conductivity of GaAs/AlAs superlattices. *Phys. B* **219–220**, 699–701 (1996).
64. Capinski, W. S. et al. Thermal-conductivity measurements of GaAs/AlAs superlattices using a picosecond optical pump-and-probe technique. *Phys. Rev. B* **59**, 8105–8113 (1999).
65. Huxtable, S., Cahill, D. G., Fauconnier, V., White, J. O. & Zhao, J. C. Thermal conductivity imaging at micrometre-scale resolution for combinatorial studies of materials. *Nat. Mater.* **3**, 298–301 (2004).
66. Cahill, D. G. et al. Nanoscale thermal transport. *J. Appl. Phys.* **93**, 793–818 (2003).
67. Costescu, R. M., Wall, M. A. & Cahill, D. G. Thermal conductance of epitaxial interfaces. *Phys. Rev. B* **67**, 054302 (2003).
This work demonstrates using TDTR to measure the thermal interface conductance.
68. Koh, Y. K. et al. Comparison of the 3ω method and time-domain thermoreflectance for measurements of the cross-plane thermal conductivity of epitaxial semiconductors. *J. Appl. Phys.* **105**, 54303 (2009).
69. Jiang, P., Qian, X. & Yang, R. Tutorial: time-domain thermoreflectance (TDTR) for thermal property characterization of bulk and thin film materials. *J. Appl. Phys.* **28**, 161103 (2018).
This paper presents an extensive tutorial on TDTR.
70. Feser, J. P. & Cahill, D. G. Probing anisotropic heat transport using time-domain thermoreflectance with offset laser spots. *Rev. Sci. Instrum.* **83**, 104901 (2012).
This work uses a configuration of TDTR with offset pump and probe to measure both in-plane and out-of-plane thermal conductivity of materials.
71. Feser, J. P., Liu, J. & Cahill, D. G. Pump–probe measurements of the thermal conductivity tensor for materials lacking in-plane symmetry. *Rev. Sci. Instrum.* **85**, 104903 (2014).
72. Kimling, J., Philippi-Kobs, A., Jacobsohn, J., Oepen, H. P. & Cahill, D. G. Thermal conductance of interfaces with amorphous SiO_2 measured by time-resolved magneto-optic Kerr-effect thermometry. *Phys. Rev. B* **95**, 184305 (2017).
73. Angeles, F. et al. Picosecond magneto-optic thermometry measurements of nanoscale thermal transport in AlN thin films. *APL Mater.* **11**, 061127 (2023).
This study presents an example of using TR-MOKE to interrogate the cross-plane thermal conductivity of high-*k* thin films.
74. Peng, W. & Wilson, R. B. Thermal model for time-domain thermoreflectance experiments in a laser-flash geometry. *J. Appl. Phys.* **131**, 134301 (2022).
This work discusses the laser-flash TDTR experiment and analyses.
75. Peng, W. & Wilson, R. B. Nanoscale laser flash measurements of diffuson transport in amorphous Ge and Si. *APL Mater.* **10**, 041111 (2022).
76. Losego, M. D., Grady, M. E., Sottos, N. R., Cahill, D. G. & Braun, P. V. Effects of chemical bonding on heat transport across interfaces. *Nat. Mater.* **11**, 502–506 (2012).
77. Zheng, X., Cahill, D. G. & Zhao, J.-C. Effect of MeV ion irradiation on the coefficient of thermal expansion of Fe–Ni invar alloys: a combinatorial study. *Acta Mater.* **58**, 1236–1241 (2010).

78. Zheng, X., Cahill, D. G., Weaver, R. & Zhao, J.-C. Micron-scale measurements of the coefficient of thermal expansion by time-domain probe beam deflection. *J. Appl. Phys.* **104**, 73509 (2008).
This work presents as explanation of probe-beam deflection effects in TDTR experiments.
79. Tomko, J. A. et al. Nanoscale wetting and energy transmission at solid/liquid interfaces. *Langmuir* **35**, 2106–2114 (2019).
80. Sun, J. et al. Probe beam deflection technique with liquid immersion for fast mapping of thermal conductance. *Appl. Phys. Lett.* **124**, 42201 (2024).
81. Sun, J., Lv, G. & Cahill, D. G. Frequency-domain probe beam deflection method for measurement of thermal conductivity of materials on micron length scale. *Rev. Sci. Instrum.* **94**, 14903 (2023).
82. Schmidt, A. J. *Optical Characterization of Thermal Transport from the Nanoscale to the Macroscale* (Massachusetts Institute of Technology, 2008).
83. Gomez, M. J., Liu, K., Lee, J. G. & Wilson, R. B. High sensitivity pump-probe measurements of magnetic, thermal, and acoustic phenomena with a spectrally tunable oscillator. *Rev. Sci. Instrum.* **91**, 023905 (2020).
84. Liu, J., Choi, G.-M. & Cahill, D. G. Measurement of the anisotropic thermal conductivity of molybdenum disulfide by the time-resolved magneto-optic Kerr effect. *J. Appl. Phys.* **116**, 233107 (2014).
85. Jang, H. et al. Thermal conductivity of oxide tunnel barriers in magnetic tunnel junctions measured by ultrafast thermoreflectance and magneto-optic Kerr effect thermometry. *Phys. Rev. Appl.* **13**, 024007 (2020).
86. Wilson, R. B., Apgar, B. A., Martin, L. W. & Cahill, D. G. Thermoreflectance of metal transducers for optical pump–probe studies of thermal properties. *Opt. Express* **20**, 28829–28838 (2012).
87. Hohensee, G. T., Hsieh, W. P., Losego, M. D. & Cahill, D. G. Interpreting picosecond acoustics in the case of low interface stiffness. *Rev. Sci. Instrum.* **83**, 114902 (2012).
88. Wilson, R. B., Feser, J. P., Hohensee, G. T. & Cahill, D. G. Two-channel model for nonequilibrium thermal transport in pump–probe experiments. *Phys. Rev. B* **88**, 144305 (2013).
89. Yang, J., Ziade, E. & Schmidt, A. J. Modeling optical absorption for thermoreflectance measurements. *J. Appl. Phys.* **119**, 095107 (2016).
90. Hopkins, P. E. et al. Criteria for cross-plane dominated thermal transport in multilayer thin film systems during modulated laser heating. *J. Heat. Transf.* **132**, 081302 (2010).
91. Schmidt, A. J., Chen, X. & Chen, G. Pulse accumulation, radial heat conduction, and anisotropic thermal conductivity in pump–probe transient thermoreflectance. *Rev. Sci. Instrum.* **79**, 114902 (2008).
92. Wang, Y., Park, J. Y., Koh, Y. K. & Cahill, D. G. Thermoreflectance of metal transducers for time-domain thermoreflectance. *J. Appl. Phys.* **108**, 43507 (2010).
93. Rosei, R., Colavita, E., Franciosi, A., Weaver, J. H. & Peterson, D. T. Electronic structure of the bcc transition metals: thermoreflectance studies of bulk V, Nb, Ta, and αTaH_x. *Phys. Rev. B* **21**, 3152–3157 (1980).
94. Islam, M. R. et al. Evaluating size effects on the thermal conductivity and electron-phonon scattering rates of copper thin films for experimental validation of Matthiessen's rule. *Nat. Commun.* **15**, 9167 (2024).
95. Yang, J., Ziade, E. & Schmidt, A. J. Uncertainty analysis of thermoreflectance measurements. *Rev. Sci. Instrum.* **87**, 014901 (2016).
96. Khan, S., Shi, X., Feser, J. & Wilson, R. Thermal conductance of interfaces between titanium nitride and group IV semiconductors at high temperatures. *Appl. Phys. Lett.* **125**, 041601 (2024).
97. Khan, S. et al. Properties for thermally conductive interfaces with wide band gap materials. *ACS Appl. Mater. Interfaces* **14**, 36178–36188 (2022).
98. Jiang, P., Huang, B. & Koh, Y. K. Accurate measurements of cross-plane thermal conductivity of thin films by dual-frequency time-domain thermoreflectance (TDTR). *Rev. Sci. Instrum.* **87**, 075101 (2016).
99. Kan, Y. K. *Heat Transport by Phonons in Crystalline Materials and Nanostructures* (Univ. of Illinois at Urbana-Champaign, 2010).
100. Cheng, Z. et al. Thermal visualization of buried interfaces enabled by ratio signal and steady-state heating of time-domain thermoreflectance. *ACS Appl. Mater. Interfaces* **13**, 31843–31851 (2021).
101. Szwejkowski, C. J. et al. Size effects in the thermal conductivity of gallium oxide (β-Ga_2O_3) films grown via open-atmosphere annealing of gallium nitride. *J. Appl. Phys.* **117**, 084308 (2015).
102. Aryana, K. et al. Interface controlled thermal resistances of ultra-thin chalcogenide-based phase change memory devices. *Nat. Commun.* **12**, 774 (2021).
103. Lee, S.-M. & Cahill, D. G. Heat transport in thin dielectric films. *J. Appl. Phys.* **81**, 2590–2595 (1997).
104. Jiang, P., Qian, X., Yang, R. & Lindsay, L. Anisotropic thermal transport in bulk hexagonal boron nitride. *Phys. Rev. Mater.* **2**, 064005 (2018).
105. Jiang, P., Qian, X. & Yang, R. Time-domain thermoreflectance (TDTR) measurements of anisotropic thermal conductivity using a variable spot size approach. *Rev. Sci. Instrum.* **88**, 074901 (2017).
106. Rai, A., Sangwan, V. K., Gish, J. T., Hersam, M. C. & Cahill, D. G. Anisotropic thermal conductivity of layered indium selenide. *Appl. Phys. Lett.* **118**, 073101 (2021).
107. Jiang, P., Qian, X. & Yang, R. A new elliptical-beam method based on time-domain thermoreflectance (TDTR) to measure the in-plane anisotropic thermal conductivity and its comparison with the beam-offset method. *Rev. Sci. Instrum.* **89**, 094902 (2018).
108. Zhu, J. et al. Revealing the origins of 3D anisotropic thermal conductivities of black phosphorus. *Adv. Electron. Mater.* **2**, 1600040 (2016).
109. Jang, H., Wood, J. D., Ryder, C. R., Hersam, M. C. & Cahill, D. G. Anisotropic thermal conductivity of exfoliated black phosphorus. *Adv. Mater.* **27**, 8017–8022 (2015).
110. Braun, J. L., Olson, D. H., Gaskins, J. T. & Hopkins, P. E. A steady-state thermoreflectance method to measure thermal conductivity. *Rev. Sci. Instrum.* **90**, 24905 (2019).
This work reviews SSTR.
111. Oh, D.-W., Ko, C., Ramanathan, S. & Cahill, D. G. Thermal conductivity and dynamic heat capacity across the metal-insulator transition in thin film VO_2. *Appl. Phys. Lett.* **96**, 151906 (2010).
112. Olson, D. H., Braun, J. L. & Hopkins, P. E. Spatially resolved thermoreflectance techniques for thermal conductivity measurements from the nanoscale to the mesoscale. *J. Appl. Phys.* **126**, 150901 (2019).
113. Wang, X., Liman, C. D., Treat, N. D., Chabinyc, M. L. & Cahill, D. G. Ultralow thermal conductivity of fullerene derivatives. *Phys. Rev. B* **88**, 075310 (2013).
114. Liu, J. et al. Simultaneous measurement of thermal conductivity and heat capacity of bulk and thin film materials using frequency-dependent transient thermoreflectance method. *Rev. Sci. Instrum.* **84**, 034902 (2013).
This study develops multi-frequency TDTR to measure both thermal conductivity and heat capacity.
115. Wei, C., Zheng, X., Cahill, D. G. & Zhao, J. C. Invited article: micron resolution spatially resolved measurement of heat capacity using dual-frequency time-domain thermoreflectance. *Rev. Sci. Instrum.* **84**, 071301 (2013).
116. Wilson, R. B. et al. Electric current induced ultrafast demagnetization. *Phys. Rev. B* **96**, 045105 (2017).
117. Qian, X., Zhou, J. & Chen, G. Phonon-engineered extreme thermal conductivity materials. *Nat. Mater.* **20**, 1188–1202 (2021).
118. Cheng, Z., Graham, S., Amano, H. & Cahill, D. G. Perspective on thermal conductance across heterogeneously integrated interfaces for wide and ultrawide bandgap electronics. *Appl. Phys. Lett.* **120**, 030501 (2022).
119. Zhang, Z. et al. Observation of thermal spin-transfer torque via ferromagnetic resonance in magnetic tunnel junctions. *Phys. Rev. B* **94**, 064414 (2016).
120. Choi, G.-M., Wilson, R. B. & Cahill, D. G. Indirect heating of Pt by short-pulse laser irradiation of Au in a nanoscale Pt/Au bilayer. *Phys. Rev. B* **89**, 064307 (2014).
121. Angeles, F., Shi, X. & Wilson, R. B. In situ and ex situ processes for synthesizing metal multilayers with electronically conductive interfaces. *J. Appl. Phys.* **131**, 225302 (2022).
122. Choi, G.-M., Moon, C.-H., Min, B.-C., Lee, K.-J. & Cahill, D. G. Thermal spin-transfer torque driven by the spin-dependent Seebeck effect in metallic spin-valves. *Nat. Phys.* **11**, 576–581 (2015).
123. Koh, Y. R. et al. Thermal boundary conductance across epitaxial metal/sapphire interfaces. *Phys. Rev. B* **102**, 205304 (2020).
124. Kang, J. S. et al. Integration of boron arsenide cooling substrates into gallium nitride devices. *Nat. Electron.* **4**, 416–423 (2021).
125. Cheng, Z. et al. High thermal conductivity in wafer-scale cubic silicon carbide crystals. *Nat. Commun.* **13**, 7201 (2022).
126. Mu, F. et al. High thermal boundary conductance across bonded heterogeneous GaN–SiC interfaces. *ACS Appl. Mater. Interfaces* **11**, 33428–33434 (2019).
127. Cheng, Z., Mu, F., Yates, L., Suga, T. & Graham, S. Interfacial thermal conductance across room-temperature-bonded GaN/diamond interfaces for GaN-on-diamond devices. *ACS Appl. Mater. Interfaces* **12**, 8376–8384 (2020).
128. Cheng, Z. et al. Tunable thermal energy transport across diamond membranes and diamond–Si interfaces by nanoscale graphoepitaxy. *ACS Appl. Mater. Interfaces* **11**, 18517–18527 (2019).
129. Cahill, D. G. et al. Nanoscale thermal transport. II. 2003–2012. *Appl. Phys. Rev.* **1**, 011305 (2014).
130. Giri, A. & Hopkins, P. E. A review of experimental and computational advances in thermal boundary conductance and nanoscale thermal transport across solid interfaces. *Adv. Funct. Mater.* **30**, 1903857 (2020).
131. Chen, J., Xu, X., Zhou, J. & Li, B. Interfacial thermal resistance: past, present, and future. *Rev. Mod. Phys.* **94**, 025002 (2022).
132. Wilson, R. B. & Cahill, D. G. Experimental validation of the interfacial form of the Wiedemann–Franz law. *Phys. Rev. Lett.* **108**, 255901 (2012).
133. Cheng, Z. et al. Thermal conductance across harmonic-matched epitaxial Al–sapphire heterointerfaces. *Commun. Phys.* **3**, 115 (2020).
134. Gaskins, J. T. et al. Thermal boundary conductance across heteroepitaxial ZnO/GaN interfaces: assessment of the phonon gas model. *Nano. Lett.* **18**, 7469–7477 (2018).
135. Norris, P. M. & Hopkins, P. E. Examining interfacial diffuse phonon scattering through transient thermoreflectance measurements of thermal boundary conductance. *J. Heat. Transf.* **131**, 043207 (2009).
136. Wilson, R. B., Apgar, B. A., Hsieh, W.-P., Martin, L. W. & Cahill, D. G. Thermal conductance of strongly bonded metal–oxide interfaces. *Phys. Rev. B* **91**, 115414 (2015).
137. Angeles, F. et al. Interfacial thermal transport in spin caloritronic material systems. *Phys. Rev. Mater.* **5**, 114403 (2021).
138. Hopkins, P. E. et al. Manipulating thermal conductance at metal–graphene contacts via chemical functionalization. *Nano. Lett.* **12**, 590–595 (2012).
139. Vaziri, S. et al. Ultrahigh thermal isolation across heterogeneously layered two-dimensional materials. *Sci. Adv.* **5**, eaax1325 (2019).
140. Lyeo, H.-K. & Cahill, D. G. Thermal conductance of interfaces between highly dissimilar materials. *Phys. Rev. B* **73**, 144301 (2006).

141. Hohensee, G. T., Fellinger, M. R., Trinkle, D. R. & Cahill, D. G. Thermal transport across high-pressure semiconductor-metal transition in Si and $Si_{0.991}Ge_{0.009}$. *Phys. Rev. B* **91**, 205104 (2015).
142. Dalton, D. A., Hsieh, W.-P., Hohensee, G. T., Cahill, D. G. & Goncharov, A. F. Effect of mass disorder on the lattice thermal conductivity of MgO periclase under pressure. *Sci. Rep.* **3**, 2400 (2013).
143. Hsieh, W.-P. et al. Testing the minimum thermal conductivity model for amorphous polymers using high pressure. *Phys. Rev. B* **83**, 174205 (2011).
144. Hohensee, G. T., Wilson, R. B. & Cahill, D. G. Thermal conductance of metal–diamond interfaces at high pressure. *Nat. Commun.* **6**, 6578 (2015).
145. Hsieh, W.-P., Lyons, A. S., Pop, E., Keblinski, P. & Cahill, D. G. Pressure tuning of the thermal conductance of weak interfaces. *Phys. Rev. B* **84**, 184107 (2011).
146. Hsieh, W.-P., Chen, B., Li, J., Keblinski, P. & Cahill, D. G. Pressure tuning of the thermal conductivity of the layered muscovite crystal. *Phys. Rev. B* **80**, 180302 (2009).
147. Sääskilahti, K., Oksanen, J., Tulkki, J. & Volz, S. Role of anharmonic phonon scattering in the spectrally decomposed thermal conductance at planar interfaces. *Phys. Rev. B* **90**, 134312 (2014).
148. Lu, Z., Chaka, A. M. & Sushko, P. V. Thermal conductance enhanced via inelastic phonon transport by atomic vacancies at Cu/Si interfaces. *Phys. Rev. B* **102**, 075449 (2020).
149. Stevens, R. J., Zhigilei, L. V. & Norris, P. M. Effects of temperature and disorder on thermal boundary conductance at solid–solid interfaces: nonequilibrium molecular dynamics simulations. *Int. J. Heat. Mass. Transf.* **50**, 3977–3989 (2007).
150. Dai, J. & Tian, Z. Rigorous formalism of anharmonic atomistic Green's function for three-dimensional interfaces. *Phys. Rev. B* **101**, 041301 (2020).
151. Guo, Y. et al. Anharmonic phonon–phonon scattering at the interface between two solids by nonequilibrium Green's function formalism. *Phys. Rev. B* **103**, 174306 (2021).
152. Sadasivam, S. et al. Thermal transport across metal silicide-silicon interfaces: first-principles calculations and Green's function transport simulations. *Phys. Rev. B* **95**, 085310 (2017).
153. Majumdar, A. & Reddy, P. Role of electron–phonon coupling in thermal conductance of metal–nonmetal interfaces. *Appl. Phys. Lett.* **84**, 4768–4770 (2004).
154. Sergeev, A. V. Electronic Kapitza conductance due to inelastic electron-boundary scattering. *Phys. Rev. B* **58**, R10199–R10202 (1998).
155. Sergeev, A. Inelastic electron–boundary scattering in thin films. *Phys. B Condens. Matter* **263–264**, 217–219 (1999).
156. Mahan, G. D. Kapitza thermal resistance between a metal and a nonmetal. *Phys. Rev. B* **79**, 075408 (2009).
157. Hopkins, P. E., Kassebaum, J. L. & Norris, P. M. Effects of electron scattering at metal–nonmetal interfaces on electron–phonon equilibration in gold films. *J. Appl. Phys.* **105**, 023710 (2009).
158. Wang, Y., Ruan, X. & Roy, A. K. Two-temperature nonequilibrium molecular dynamics simulation of thermal transport across metal–nonmetal interfaces. *Phys. Rev. B* **85**, 205311 (2012).
159. P. Rudolph, ed. *Handbook of Crystal Growth, Bulk Crystal Growth* Vol. II (Elsevier, 2015).
160. Li, S. et al. High thermal conductivity in cubic boron arsenide crystals. *Science* **361**, 579–581 (2018).
161. Hou, S. et al. Strong temperature dependence of thermal conductivity in high-purity cubic boron arsenide. *Phys. Rev. B* **111**, 23520 (2025).
162. Hou, S. et al. Thermal conductivity of BAs under pressure. *Adv. Electron. Mater.* **8**, 2200017 (2022).
163. Chen, K. et al. Ultrahigh thermal conductivity in isotope-enriched cubic boron nitride. *Science* **367**, 555–559 (2020).
164. Kang, J. S., Wu, H. & Hu, Y. Thermal properties and phonon spectral characterization of synthetic boron phosphide for high thermal conductivity applications. *Nano Lett.* **17**, 7507–7514 (2017).
165. Zheng, Q. et al. High thermal conductivity in isotopically enriched cubic boron phosphide. *Adv. Funct. Mater.* **28**, 1805116 (2018).
166. Lv, B. et al. Experimental study of the proposed super-thermal-conductor: BAs. *Appl. Phys. Lett.* **106**, 074105 (2015).
167. Feng, T., Lindsay, L. & Ruan, X. Four-phonon scattering significantly reduces intrinsic thermal conductivity of solids. *Phys. Rev. B* **96**, 161201 (2017).
168. Lindsay, L., Broido, D. A. & Reinecke, T. L. First-principles determination of ultrahigh thermal conductivity of boron arsenide: a competitor for diamond? *Phys. Rev. Lett.* **111**, 025901 (2013).
169. Broido, D. A., Lindsay, L. & Reinecke, T. L. Ab initio study of the unusual thermal transport properties of boron arsenide and related materials. *Phys. Rev. B* **88**, 214303 (2013).
170. Ravichandran, N. K. & Broido, D. Non-monotonic pressure dependence of the thermal conductivity of boron arsenide. *Nat. Commun.* **10**, 827 (2019).
171. Mion, C., Muth, J. F., Preble, E. A. & Hanser, D. Thermal conductivity, dislocation density and GaN device design. *Superlatt. Microstruct.* **40**, 338–342 (2006).
172. Zou, J., Kotchetkov, D., Balandin, A. A., Florescu, D. I. & Pollak, F. H. Thermal conductivity of GaN films: effects of impurities and dislocations. *J. Appl. Phys.* **92**, 2534–2539 (2002).
173. Beechem, T. E. et al. Size dictated thermal conductivity of GaN. *J. Appl. Phys.* **120**, 095104 (2016).
174. Koh, Y. R. et al. Bulk-like intrinsic phonon thermal conductivity of micrometer-thick AlN films. *ACS Appl. Mater. Interfaces* **12**, 29443–29450 (2020).
175. Sood, A. et al. Anisotropic and inhomogeneous thermal conduction in suspended thin-film polycrystalline diamond. *J. Appl. Phys.* **119**, 175103 (2016).
176. Jiang, P., Lindsay, L., Huang, X. & Koh, Y. K. Interfacial phonon scattering and transmission loss in >1 μm thick silicon-on-insulator thin films. *Phys. Rev. B* **97**, 195308 (2018).
177. Sun, B. et al. Dislocation-induced thermal transport anisotropy in single-crystal group-III nitride films. *Nat. Mater.* **18**, 136–140 (2019).
178. Cahill, D. G., Watson, S. K. & Pohl, R. O. Lower limit to the thermal conductivity of disordered crystals. *Phys. Rev. B* **46**, 6131–6140 (1992).
179. Duda, J. C., Hopkins, P. E., Shen, Y. & Gupta, M. C. Thermal transport in organic semiconducting polymers. *Appl. Phys. Lett.* **102**, 251912 (2013).
180. Giri, A. et al. Molecular tail chemistry controls thermal transport in fullerene films. *Phys. Rev. Mater.* **4**, 65404 (2020).
181. Chiritescu, C. et al. Ultralow thermal conductivity in disordered, layered WSe_2 crystals. *Science* **315**, 351–353 (2007).
This work presents an experimental realization of the lowest thermal conductivity fully dense solid at room temperature with TDTR.
182. Hadland, E. C. et al. Ultralow thermal conductivity of turbostratically disordered $MoSe_2$ ultra-thin films and implications for heterostructures. *Nanotechnology* **30**, 285401 (2019).
183. Kim, S. E. et al. Extremely anisotropic van der Waals thermal conductors. *Nature* **597**, 660–665 (2021).
184. Li, D., Schleife, A., Cahill, D. G., Mitchson, G. & Johnson, D. C. Ultralow shear modulus of incommensurate $[SnSe]_n[MoSe_2]_n$ layers synthesized by the method of modulated elemental reactants. *Phys. Rev. Mater.* **3**, 043607 (2019).
185. Hadland, E. et al. Synthesis, characterization, and ultralow thermal conductivity of a lattice-mismatched $SnSe_2(MoSe_2)_{1.32}$ heterostructure. *Chem. Mater.* **31**, 5699–5705 (2019).
186. Gunning, N. S., Feser, J., Beekman, M., Cahill, D. G. & Johnson, D. C. Synthesis and thermal properties of solid-state structural isomers: ordered intergrowths of SnSe and $MoSe_2$. *J. Am. Chem. Soc.* **137**, 8803–8809 (2015).
187. Dai, H. & Wang, R. Methods for measuring thermal conductivity of two-dimensional materials: a review. *Nanomaterials* **12**, 589 (2022).
188. Dong, Y., Wu, Z.-S., Ren, W., Cheng, H.-M. & Bao, X. Graphene: a promising 2D material for electrochemical energy storage. *Sci. Bull.* **62**, 724–740 (2017).
189. Munteanu, R.-E., Moreno, P. S., Bramini, M. & Gáspár, S. 2D materials in electrochemical sensors for in vitro or in vivo use. *Anal. Bioanal. Chem.* **413**, 701–725 (2021).
190. Wang, X. et al. Recent advances in the functional 2D photonic and optoelectronic devices. *Adv. Opt. Mater.* **7**, 1801274 (2019).
191. Jiang, P., Qian, X., Gu, X. & Yang, R. Probing anisotropic thermal conductivity of transition metal dichalcogenides MX_2 (M=Mo, W and X=S, Se) using time-domain thermoreflectance. *Adv. Mater.* **29**, 1701068 (2017).
192. Xu, K. et al. In-plane thermal diffusivity determination using beam-offset frequency-domain thermoreflectance with a one-dimensional optical heat source. *Int. J. Heat. Mass. Transf.* **214**, 124376 (2023).
193. Gu, X. & Yang, R. Phonon transport in single-layer transition metal dichalcogenides: a first-principles study. *Appl. Phys. Lett.* **105**, 131903 (2014).
194. Zhu, G. et al. Tuning thermal conductivity in molybdenum disulfide by electrochemical intercalation. *Nat. Commun.* **7**, 13211 (2016).
195. Jiang, P., Qian, X., Li, X. & Yang, R. Three-dimensional anisotropic thermal conductivity tensor of single crystalline β-Ga_2O_3. *Appl. Phys. Lett.* **113**, 232105 (2018).
196. Sood, A. et al. Direct visualization of thermal conductivity suppression due to enhanced phonon scattering near individual grain boundaries. *Nano. Lett.* **18**, 3466–3472 (2018).
197. Grimm, D. et al. Thermal conductivity of mechanically joined semiconducting/metal nanomembrane superlattices. *Nano. Lett.* **14**, 2387–2393 (2014).
198. Cheng, Z. et al. Probing local thermal conductivity variations in CVD diamond with large grains by time-domain thermoreflectance. In *Proc. Int. Heat Transf. Conf.* Vol. 16 8694–8701 (Begellhouse, 2018).
199. Sood, A. et al. An electrochemical thermal transistor. *Nat. Commun.* **9**, 4510 (2018).
200. Brown, D. B. et al. Spatial mapping of thermal boundary conductance at metal–molybdenum diselenide interfaces. *ACS Appl. Mater. Interfaces* **11**, 14418–14426 (2019).
201. Cheaito, R. et al. Thermal conductivity measurements on suspended diamond membranes using picosecond and femtosecond time-domain thermoreflectance. In *Proc. IEEE Intersoc. Conf. Therm. Thermomech. Phenom. Electron. Syst. (ITherm)* 706–710 (IEEE, 2017).
202. Zheng, X., Cahill, D., Krasnochtchekov, P., Averback, R. & Zhao, J. High-throughput thermal conductivity measurements of nickel solid solutions and the applicability of the Wiedemann–Franz law. *Acta. Mater.* **55**, 5177–5185 (2007).
203. Zhao, J.-C., Zheng, X. & Cahill, D. G. Thermal conductivity mapping of the Ni–Al system and the β-NiAl phase in the Ni–Al–Cr system. *Scr. Mater.* **66**, 935–938 (2012).
204. Germain, T., Chowdhury, T. A., Carter, J. & Putnam, S. A. Measuring heat transfer coefficients for microchannel jet impingement using time-domain thermoreflectance. In *Proc. IEEE Intersoc. Conf. Therm. Thermomech. Phenom. Electron. Syst. (ITherm)* 449–454 (IEEE, 2018).
205. Mehrvand, M. & Putnam, S. A. Probing the local heat transfer coefficient of |water-cooled microchannels using time-domain thermoreflectance. *J. Heat. Transf.* **139**, 112403 (2017).
206. Mehrvand, M. & Putnam, S. A. Transient and local two-phase heat transport at macro-scales to nano-scales. *Commun. Phys.* **1**, 21 (2018).
207. Xie, X., Diao, Z. & Cahill, D. G. Microscale, bendable thermoreflectance sensor for local measurements of the thermal effusivity of biological fluids and tissues. *Rev. Sci. Instrum.* **91**, 044903 (2020).
208. Tian, Z., Marconnet, A. & Chen, G. Enhancing solid–liquid interface thermal transport using self-assembled monolayers. *Appl. Phys. Lett.* **106**, 211602 (2015).

209. Ge, Z., Cahill, D. G. & Braun, P. V. Thermal conductance of hydrophilic and hydrophobic interfaces. *Phys. Rev. Lett.* **96**, 186101 (2006).
This work measures the thermal boundary conductance across solid–liquid interfaces with TDTR.
210. Hsieh, W. P. & Deschamps, F. Thermal conductivity of H_2O–CH_3OH mixtures at high pressures: implications for the dynamics of icy super-Earths outer shells. *J. Geophys. Res. Planets* **120**, 1697–1707 (2015).
211. Yong Park, J., Gardner, A., King, W. P. & Cahill, D. G. Droplet impingement and vapor layer formation on hot hydrophobic surfaces. *J. Heat. Transf.* **136**, 092902 (2014).
212. Yong Park, J., Min, C.-K., Granick, S. & Cahill, D. G. Residence time and heat transfer when water droplets hit a scalding surface. *J. Heat. Transf.* **134**, 101503 (2012).
213. Shin, J. et al. Thermally functional liquid crystal networks by magnetic field driven molecular orientation. *ACS Macro. Lett.* **5**, 955–960 (2016).
214. Ueji, K. et al. In situ time-domain thermoreflectance measurements using Au as the transducer during electrolyte gating. *Appl. Phys. Lett.* **117**, 133104 (2020).
215. Zhang, D.-L. et al. High-frequency magnetoacoustic resonance through strain–spin coupling in perpendicular magnetic multilayers. *Sci. Adv.* **6**, eabb4607 (2020).
216. Chen, B., Hsieh, W. P., Cahill, D. G., Trinkle, D. R. & Li, J. Thermal conductivity of compressed H_2O to 22 GPa: a test of the Leibfried–Schlömann equation. *Phys. Rev. B* **83**, 132301 (2011).
217. Ortiz, V. H. et al. Thermal conductivity of irradiated tetragonal lithium aluminate. *J. Nucl. Mater.* **606**, 155585 (2025).
218. Cheaito, R., Gorham, C. S., Misra, A., Hattar, K. & Hopkins, P. E. Thermal conductivity measurements via time-domain thermoreflectance for the characterization of radiation induced damage. *J. Mater. Res.* **30**, 1403–1412 (2015).
219. Alaie, S. et al. Reduction and increase in thermal conductivity of Si irradiated with Ga^+ via focused ion beam. *ACS Appl. Mater. Interfaces* **10**, 37679–37684 (2018).
220. Pfeifer, T. W. et al. Measuring sub-surface spatially varying thermal conductivity of silicon implanted with krypton. *J. Appl. Phys.* **132**, 075112 (2022).
This work demonstrates resolving the thermal conductivity as a function of depth of irradiated silicon with TDTR.
221. Scott, E. A. et al. Orders of magnitude reduction in the thermal conductivity of polycrystalline diamond through carbon, nitrogen, and oxygen ion implantation. *Carbon* **157**, 97–105 (2020).
222. Scott, E. A. et al. Reductions in the thermal conductivity of irradiated silicon governed by displacement damage. *Phys. Rev. B* **104**, 134306 (2021).
223. Scott, E. A. et al. Phonon scattering effects from point and extended defects on thermal conductivity studied via ion irradiation of crystals with self-impurities. *Phys. Rev. Mater.* **2**, 095001 (2018).
224. Scott, E. A. et al. Thermal conductivity enhancement in ion-irradiated hydrogenated amorphous carbon films. *Nano Lett.* **21**, 3935–3940 (2021).
225. Pfeifer, T. W. et al. Ion irradiation induced crystalline disorder accelerates interfacial phonon conversion and reduces thermal boundary resistance. *Phys. Rev. B* **109**, 165421 (2024).
226. Gorham, C. S. et al. Ion irradiation of the native oxide/silicon surface increases the thermal boundary conductance across aluminum/silicon interfaces. *Phys. Rev. B* **90**, 024301 (2014).
227. Hopkins, P. E. et al. Influence of anisotropy on thermal boundary conductance at solid interfaces. *Phys. Rev. B* **84**, 125408 (2011).
228. Hopkins, P. E. et al. Reduction in thermal boundary conductance due to proton implantation in silicon and sapphire. *Appl. Phys. Lett.* **98**, 231901 (2011).
229. Zheng, X. & Eng, B. *High-throughput Measurements of Thermal Conductivity and the Coefficient of Thermal Expansion* (Univ. of Illinois at Urbana-Champaign, 2008).
230. Rost, C. M. et al. Hafnium nitride films for thermoreflectance transducers at high temperatures: potential based on heating from laser absorption. *Appl. Phys. Lett.* **111**, 151902 (2017).
231. Wilson, R. B. & Cahill, D. G. Anisotropic failure of Fourier theory in time-domain thermoreflectance experiments. *Nat. Commun.* **5**, 5075 (2014).
This work presents a set of comprehensive measurements, analyses and discussion of 'mean free path spectroscopy' effects in TDTR measurements.
232. Minnich, A. J. et al. Thermal conductivity spectroscopy technique to measure phonon mean free paths. *Phys. Rev. Lett.* **107**, 095901 (2011).
233. Koh, Y. K. & Cahill, D. G. Frequency dependence of the thermal conductivity of semiconductor alloys. *Phys. Rev. B* **76**, 075207 (2007).
234. Regner, K. T. et al. Broadband phonon mean free path contributions to thermal conductivity measured using frequency domain thermoreflectance. *Nat. Commun.* **4**, 1640 (2013).
235. Wilson, R. B. & Cahill, D. G. Limits to Fourier theory in high thermal conductivity single crystals. *Appl. Phys. Lett.* **107**, 203112 (2015).
236. Vermeersch, B., Mohammed, A. M. S., Pernot, G., Koh, Y. R. & Shakouri, A. Superdiffusive heat conduction in semiconductor alloys. II. Truncated Lévy formalism for experimental analysis. *Phys. Rev. B* **91**, 085203 (2015).
237. Vermeersch, B., Carrete, J., Mingo, N. & Shakouri, A. Superdiffusive heat conduction in semiconductor alloys. I. Theoretical foundations. *Phys. Rev. B* **91**, 085202 (2015).
238. Li, X., Han, J. & Lee, S. Thermal resistance from non-equilibrium phonons at Si–Ge interface. *Mater. Today Phys.* **34**, 101063 (2023).
239. Han, J. & Lee, S. Thermal resistance across Si–SiGe alloy interface from phonon distribution mismatch. *Appl. Phys. Lett.* **124**, 142201 (2024).
240. Han, J. & Lee, S. Nonequilibrium thermal resistance of interfaces between III–V compounds. *Phys. Rev. Mater.* **8**, 014604 (2024).
241. Hua, C., Chen, X., Ravichandran, N. K. & Minnich, A. J. Experimental metrology to obtain thermal phonon transmission coefficients at solid interfaces. *Phys. Rev. B* **95**, 205423 (2017).
242. Hoque, M. S. B. et al. High in-plane thermal conductivity of aluminum nitride thin films. *ACS Nano* **15**, 9588–9599 (2021).
243. Tadjer, M. J. et al. Effect of GaN/AlGaN buffer thickness on the electrothermal performance of AlGaN/GaN high electron mobility transistors on engineered substrates. *Phys. Status Solidi A* **220**, 2200828 (2023).
244. Hoque, M. S. B. et al. Connection length controlled sound speed and thermal conductivity of hybrid metalcone films. *Nano Lett.* **25**, 2594–2599 (2025).
245. Aller, H. T. et al. Low thermal resistance of diamond–AlGaN interfaces achieved using carbide interlayers. *Adv. Mater. Interfaces* **12**, 2400575 (2025).
246. Pfeifer, T. W. et al. Limitations and advances in optical thermometry: nanoscale resistances, ultrahigh thermal conductivity, and ultrahigh temperatures. *Annu. Rev. Mater. Res.* **55**, 080423-010435 (2025).
247. Hopkins, P. E. et al. Effect of dislocation density on thermal boundary conductance across GaSb/GaAs interfaces. *Appl. Phys. Lett.* **98**, 161913 (2011).
248. Chen, G. Nonlocal and nonequilibrium heat conduction in the vicinity of nanoparticles. *J. Heat. Transf.* **118**, 539 (1996).
249. Braun, J. L., Szwejkowski, C. J., Giri, A. & Hopkins, P. E. On the steady-state temperature rise during laser heating of multilayer thin films in optical pump–probe techniques. *J. Heat. Transf.* **140**, 052801 (2018).
250. Scott, E. A. et al. Probing thermal conductivity of subsurface, amorphous layers in irradiated diamond. *J. Appl. Phys.* **129**, 055307 (2021).
251. Bin Hoque, Md. S. et al. Thermal conductivity measurements of sub-surface buried substrates by steady-state thermoreflectance. *Rev. Sci. Instrum.* **92**, 64906 (2021).
252. Salnick, A. & Opsal, J. Dynamics of the plasma and thermal waves in surface-modified semiconductors. *Rev. Sci. Instrum.* **74**, 545–549 (2003).
253. Schmidt, A. J., Cheaito, R. & Chiesa, M. A frequency-domain thermoreflectance method for the characterization of thermal properties. *Rev. Sci. Instrum.* **80**, 94901 (2009).
This work introduces the development of FDTR.
254. Schmidt, A. J., Cheaito, R. & Chiesa, M. Characterization of thin metals films via frequency-domain thermoreflectance. *J. Appl. Phys.* **107**, 24908 (2010).
255. Regner, K. T., Majumdar, S. & Malen, J. A. Instrumentation of broadband frequency domain thermoreflectance for measuring thermal conductivity accumulation functions. *Rev. Sci. Instrum.* **84**, 64901 (2013).
256. Ziade, E. Wide bandwidth frequency-domain thermoreflectance: volumetric heat capacity, anisotropic thermal conductivity, and thickness measurements. *Rev. Sci. Instrum.* **91**, 124901 (2020).
257. Ziade, E. et al. Thickness dependent thermal conductivity of gallium nitride. *Appl. Phys. Lett.* **110**, 31903 (2017).
258. Scott, E. A. et al. Thermal conductivity of $(Ge_2Sb_2Te_5)_{1-x}C_x$ phase change films. *J. Appl. Phys.* **128**, 155106 (2020).
259. Kirsch, D. J. et al. An instrumentation guide to measuring thermal conductivity using frequency domain thermoreflectance (FDTR). *Rev. Sci. Instrum.* **95**, 103006 (2024).
260. Xiang, Z., Pang, Y., Qian, X. & Yang, R. Machine learning reconstruction of depth-dependent thermal conductivity profile from pump–probe thermoreflectance signals. *Appl. Phys. Lett.* **122**, 142201 (2023).
This work uses machine learning to analyse TDTR data.
261. Shen, W., Vaca, D. & Kumar, S. Reconsidering uncertainty from frequency domain thermoreflectance measurement and novel data analysis by deep learning. *Nanoscale Microscale Thermophys. Eng.* **24**, 138–149 (2020).
262. Hodges, W., Jarzembski, A., McDonald, A., Ziade, E. & Pickrell, G. W. Sensing depths in frequency domain thermoreflectance. *J. Appl. Phys.* **131**, 245103 (2022).
263. Delmas, W. et al. Thermal transport and mechanical stress mapping of a compression bonded GaN/diamond interface for vertical power devices. *ACS Appl. Mater. Interfaces* **16**, 11003–11012 (2024).
264. Zandavi, S. H., Schmidt, A. & Brun, X. Assessing thermal resistance in fusion bond layers of 3D heterogeneous electronics packaging. *J. Appl. Phys.* **136**, 155303 (2024).
265. Poopakdee, N., Abdallah, Z., Pomeroy, J. W. & Kuball, M. In situ thermoreflectance characterization of thermal resistance in multilayer electronics packaging. *ACS Appl. Electron. Mater.* **4**, 1558–1566 (2022).
266. Wang, L., Cheaito, R., Braun, J. L., Giri, A. & Hopkins, P. E. Thermal conductivity measurements of non-metals via combined time- and frequency-domain thermoreflectance without a metal film transducer. *Rev. Sci. Instrum.* **87**, 094902 (2016).
This study extends TDTR to probe thermal properties without a metal film transducer (such as 'transducerless' TDTR).
267. Hutchins, W. et al. Ultrafast evanescent heat transfer across solid interfaces via hyperbolic phonon polaritons in hexagonal boron nitride. *Nat. Mater.* **24**, 698–706 (2025).
268. Folland, T. G., Nordin, L., Wasserman, D. & Caldwell, J. D. Probing polaritons in the mid- to far-infrared. *J. Appl. Phys.* **125**, 191102 (2019).
269. Hutchins, W. D., Zare, S., Hirt, D., Golightly, E. & Hopkins, P. E. Infrared phonon thermoreflectance in polar dielectrics. Preprint at https://arxiv.org/abs/2504.05675 (2025).
270. Majumdar, A. Scanning thermal microscopy. *Annu. Rev. Mater. Sci.* **29**, 505–585 (1999).
271. Zhang, Y. et al. A review on principles and applications of scanning thermal microscopy (SThM). *Adv. Funct. Mater.* **30**, 1900892 (2020).
272. Siemens, M. E. et al. Quasi-ballistic thermal transport from nanoscale interfaces observed using ultrafast coherent soft X-ray beams. *Nat. Mater.* **9**, 26–30 (2010).
273. Hu, Y., Zeng, L., Minnich, A. J., Dresselhaus, M. S. & Chen, G. Spectral mapping of thermal conductivity through nanoscale ballistic transport. *Nat. Nanotechnol.* **10**, 701–706 (2015).

274. Kwon, H., Perez, C., Park, W., Asheghi, M. & Goodson, K. E. Thermal characterization of metal–oxide interfaces using time-domain thermoreflectance with nanograting transducers. *ACS Appl. Mater. Interfaces* **13**, 58059–58065 (2021).
275. Höppener, C. et al. Tip-enhanced Raman scattering. *Nat. Rev. Methods Primers* **4**, 47 (2024).
276. Caldwell, J. D. et al. Low-loss, infrared and terahertz nanophotonics using surface phonon polaritons. *Nanophotonics* **4**, 44–68 (2015).
277. Eichfeld, D. A., Maniyara, R. A., Robinson, J. A., Foley, B. M. & Ramos-Alvarado, B. A novel approach to measuring local mechanical properties via photothermal excitation of an atomic force microscope probe using an optical pump–probe inspired design. *AIP Adv.* **13**, 105035 (2023).
278. Zhang, Y., Zhu, Q. & Borca-Tasciuc, T. Thermal conductivity measurements of thin films by non-contact scanning thermal microscopy under ambient conditions. *Nanoscale Adv.* **3**, 692–702 (2021).
279. Foley, B. M., Gaskins, J. T. & Hopkins, P. E. Fiber-optic based thermal reflectance material property measurement system and related methods. US Patent 10928317 B2 (2021).
280. Malen, J. A. et al. Optical measurement of thermal conductivity using fiber aligned frequency domain thermoreflectance. *J. Heat. Transf.* **133**, 081601 (2011).
281. Dennett, C. A., Buller, D. L., Hattar, K. & Short, M. P. Real-time thermomechanical property monitoring during ion beam irradiation using in situ transient grating spectroscopy. *Nucl. Instrum. Methods Phys. Res. B* **440**, 126–138 (2019).
282. Reza, A. et al. Non-contact, non-destructive mapping of thermal diffusivity and surface acoustic wave speed using transient grating spectroscopy. *Rev. Sci. Instrum.* **91**, 054902 (2020).

Acknowledgements

Work by R.M. and P.E.H. was supported as part of the 3D Ferroelectric Microelectronics Manufacturing (3DFeM2), an Energy Frontier Research Center funded by the US Department of Energy, Office of Science, Office of Basic Energy Sciences Energy Frontier Research Centers programme under award number DE-SC0021118. Work by S.K. and R.B.W. was supported as part of ULTRA, an Energy Frontier Research Center funded by the US Department of Energy, Office of Science, Basic Energy Sciences, under award number DE-SC0021230.

Author contributions

All authors contributed to each section, and reviewed and edited the manuscript before submission.

Competing interests

P.E.H. is co-founder of Laser Thermal Analysis, Inc., a company that has commercialized frequency-domain thermoreflectance (FDTR) and steady-state thermoreflectance (SSTR) instruments. The other authors declare no competing interests.

Additional information

Supplementary information The online version contains supplementary material available at https://doi.org/10.1038/s43586-025-00425-8.

Peer review information *Nature Reviews Methods Primers* thanks Juan Sebastián Reparaz and the other, anonymous, reviewer(s) for their contribution to the peer review of this work.